Simulation of two-phase flow in 3D fractured reservoirs using a projection-based Embedded Discrete Fracture Model on Unstructured tetrahedral grids (pEDFM-U)

Cavalcante, Túlio de M.; Souza, Artur C.R.; Hajibeygi, Hadi; Carvalho, Darlan K.E.; Lyra, Paulo R.M.

DOI
10.1016/j.advwatres.2024.104679

Publication date
2024

Document Version
Final published version

Published in
Advances in Water Resources

Advances in Water Resources 187 (2024) 104679

Contents lists available at ScienceDirect

Advances in Water Resources

journal homepage: www.elsevier.com/locate/advwatres

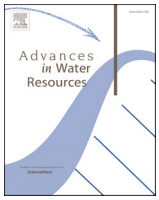

Simulation of two-phase flow in 3D fractured reservoirs using a projection-based Embedded Discrete Fracture Model on Unstructured tetrahedral grids (pEDFM-U)

Túlio de M. Cavalcante [a,*], Artur C.R. Souza [b], Hadi Hajibeygi [b], Darlan K.E. Carvalho [c], Paulo R. M. Lyra [c]

[a] Department of Civil Engineering, UFPE, Postal address: Rua Acadêmico Hélio Ramos s/n, Cidade Universitária. CEP 50.740-530, Recife, PE, Brazil
[b] Faculty of Civil Engineering and Geosciences, TUDelft. Postal address: Building 23 Stevinweg 1 2628 CN Delft, the Netherlands
[c] Department of Mechanical Engineering, UFPE, Postal address: Av. da Arquitetura s/n, 2° Andar do Bloco Escolar. CEP 50740-550, Recife, PE, Brazil

ARTICLE INFO

Keywords:
Naturally fractured reservoirs
Unstructured tetrahedral meshes
Multipoint flux approximation (MPFA)
Projection-based embedded discrete fracture model (pEDFM)

ABSTRACT

The modeling of fluid flow in heterogeneous, anisotropic and fractured porous media is relevant in many applications, including hydrocarbon and groundwater extraction, dispersion of contaminants, hydrogen or carbon dioxide (CO_2) storage. Thus, accurate and scalable simulation of fluid flow through these formations continues to be a great challenge. The presence of fractures that are explicitly modeled, ranging from flow barriers to highly conductive channels, significantly increases the complexity of the numerical simulation. The Embedded Discrete Fracture Model (EDFM) produces results that can be as accurate as those obtained using equidimensional Discrete Fracture Models (DFM) at a much lower computational cost for highly conductive fractures, but it is not adequate for impermeable barriers. In contrast, the pEDFM (projection-based Embedded Discrete Fracture Model) produces accurate results for both, channels and barriers by using additional matrix-fracture connectivities. In its current versions, it is restricted to cartesian and corner-point grid geometries and to the classical Two Point Flux Approximation (TPFA) scheme. In this work, for the first time, the pEDFM is extended to handle unstructured tetrahedral meshes (pEDFM-U). In addition, interface fluxes are approximated by using the Multipoint Flux Approximation method with a Diamond stencil (MPFA-D). This allows for simulation of highly heterogeneous and anisotropic geo-models. The developed method is robust and can deal with full permeability tensors on arbitrary tetrahedral meshes. The advective terms are discretized considering an implicit First Order Upwind (FOU) method. Our method is implemented within the DARSim (Delft Advanced Reservoir Simulation) open-source simulator framework. Through several test cases, the proposed method showed to be robust and capable to accurately capture the effects of both high and low permeability fractures for general tetrahedral meshes, under arbitrary heterogeneous and anisotropic permeability tensors for the rock matrix.

1. Introduction

Understanding the fluid flow in subsurface porous rocks is very important for a variety of applications, including hydrocarbon recovery, groundwater extraction, dispersion of contaminants and subsurface storage of hydrogen (Hassanpouryouzband et al., 2022) or carbon dioxide (CO_2) (Hassanpouryouzband et al., 2019). In this context, the computational simulation of these phenomena is essential for efficient and safe operations. Despite being crucial, modeling multiphase flow in this type of media is very challenging, due to the highly contrasting geometrical and hydrogeological properties, such as permeability (Crumpton et al., 1995; Carvalho et al., 2009). These depositional geo-environments are indeed heterogeneous and anisotropic, since the sedimentary layers can be deposited in different ways and subjected to a variety of geological processes, giving different preferential directions to the fluid flows (Carvalho et al., 2009), being particularly difficult to efficiently build structured meshes to discretize these domains (Aavatsmark et al., 1998). Moreover, the presence of fractures, ranging from flow barriers to highly conductive channels, significantly increases the complexity of the numerical simulation, so that a computational tool

* Corresponding author.
E-mail address: tulio.mcavalcante@gmail.com (T.M. Cavalcante).

https://doi.org/10.1016/j.advwatres.2024.104679
Received 5 July 2023; Received in revised form 18 March 2024; Accepted 20 March 2024
Available online 20 March 2024

projected to be used in these circumstances must adequately treat these issues.

Over the last few decades, many strategies have been developed to handle the fractures in the context of the simulation of fluid flow in porous media. Among them, traditional methods, which do not treat the fractures as additional degrees of freedom, have some remarkable limitations. Transmissibility multipliers, for example, are very dependent on the mesh (Manzocchi et al., 1999; Nilsen et al., 2012); Dual-continuum models (Barenblatt et al., 1960; Warren and Root, 1963; Dershowitz et al., 1998) need a very complex basis of parameters to guarantee a precise solution and still are not capable to deal with high fracture density and localized anisotropy (Moinfar et al., 2011). On the other hand, the models that represent fractures explicitly may be more accurate and consistent (Hoteit and Firoozabadi, 2008). Besides, the explicit discrete fracture representation may be more suitable for multiphase flow problems, because the constitutive relations for capillary pressures and relative permeabilities can be included directly in the models (Berre et al., 2019).

Explicit fracture representation methods can be divided into two families, based on the type of discretization method: conforming and non-conforming meshes. For the first group, the mesh needs to accommodate the fracture positions, which are placed at the cell edges (in 2D) or faces (in 3D). This condition is critical when it is necessary to discretize small angles and small distances and can lead to excessive local mesh refinements or distorted cells, which can be detrimental to the applied numerical formulation. This is not necessary for the second one, in which the fractures may cross the rock matrix mesh cells, which makes it simpler on the one hand, but makes it dependent of complex computational geometry calculation on the other, as this text is going to demonstrate later.

The second family is less restrictive in terms of mesh construction. In this context, there are the Embedded Discrete Fracture Models (EDFM) (Li and Lee, 2008; Hajibeygi et al., 2011; Moinfar et al., 2014; Shakiba and Sepehrnoori, 2015), in which the degrees of freedom of the rock matrix and fractures are discretized separately, and independently, and it is necessary to calculate the fluid transport between matrix and fracture. However, in the EDFM, we do not use general transfer functions based on effective parameters as in the dual-continuum methods, and it is necessary to systematically determine each "matrix cell to fracture cell" coupling in terms of the discrete variables directly (Berre et al., 2019) and based on the fracture characteristics (Moinfar et al., 2011).

The EDFM solutions are accurate for high permeability fractures, nonetheless, their application is limited whenever the fracture permeability is much lower than the rock matrix one (Ţene et al., 2017). In order to overcome the limitations of EDFM, the Projection-based Embedded Discrete Fracture Model (pEDFM) was developed by Ţene et al. (2017) and later applied to different applications (Jiang and Younis, 2017; Rao et al., 2020). pEDFM is based on the projections of the fractures on some faces of the cells in which they are contained. This strategy computes the interaction of the fractures with the cells neighboring those in which they are contained, moreover allows a fracture to influence the interaction between the cell where it is contained and its neighboring cells, enriching the model.

The pEDFM itself also evolved to overcome other limitations. From the original method of Ţene et al. (2017), Jiang and Younis (Jiang and Younis, 2017) proposed a modified formula for the effective flow area of the matrix-matrix connections and a modified fracture-matrix transmissibility calculation to avoid the flow between a fracture contained in an ultra-low permeability cell and its neighboring cells. Rao et al. (Rao et al., 2020) proposed another modification of the fracture-matrix transmissibility calculation to avoid the flow from a high permeability fracture through a neighbor cell containing a ultra-low permeability fracture, and included fracture-fracture interactions in their model, enriching the pEDFM again, beyond presenting a new strategy to choose the cell face for the fractures areas projections. The pEDFM was also extended to multilevel multiscale framework in a 3D Cartesian mesh (HosseiniMehr et al., 2020) and it has been recently extended to simulation of multiphase flow and geothermal heat in real-field applications using Corner-Point-Grid (CPG) geometries which can be also non-matching (HosseiniMehr et al., 2022).

In this context, in the present work, for the first time in literature, a simplified version of the pEDFM is extended to handle unstructured tetrahedral meshes (pEDFM-U). Here, we consider isothermal and immiscible two-phase flow of oil and water in heterogeneous, anisotropic and naturally fractured porous media. The Finite Volume Method (FVM) is used for the discretization of the continuum domain. The set of the nonlinear equations are coupled and solved using Fully Implicit Method (FIM). The matrix-matrix flux term in the mass conservation equation is discretized with a multipoint flux approximation with a diamond stencil (MPFA-D) (Lira Filho et al., 2021) and the time discretization uses a backward (implicit) Euler scheme. Additionally, for the advective terms we apply the First Order Upwind (FOU) scheme (Chen et al., 2006). The final non-linear system of algebraic equations is then solved by the Newton-Raphson (NR) method. Our formulation was implemented using the framework of the software DARSim (Delft Advanced Reservoir Simulation) which is written using MATLAB. In our formulation Through several test cases, our pEDFM-U showed to be robust and capable to accurately capture the effects of both high and low permeability fractures for general tetrahedral meshes, under arbitrary heterogeneous and anisotropic permeability tensors for the rock matrix.

2. Mathematical formulation

In this section, we present the governing equations for isothermal and immiscible two-phase flow in naturally fractured porous media. Considering a domain Ω_m representing a 3-D rock matrix intersected by fractures, it is possible to write the mass conservation equation for each phase, so that the terms related to the rock matrix are indicated by the index m and those related to the k-th fracture intersecting the domain are indicated by the index f_k. Thus, for phase α, with α = o (oil) and w (water), we can write the following expression:

$$\frac{\partial}{\partial t}(\phi\rho_\alpha S_\alpha)_m + \nabla\cdot\left(\rho_\alpha \vec{v}_\alpha\right)_m = (\rho_\alpha q_\alpha)_m + \sum_{k=1}^{n_{frac}} (\rho_\alpha \varphi_\alpha)_{m,f_k} \tag{1}$$

in which $\vec{v}_\alpha$ is the Darcy velocity, which is given by $\vec{v}_\alpha = -\lambda_\alpha \mathrm{K}(\nabla p - \rho_\alpha \vec{g})$ where the mobility is given by $\lambda_\alpha = k_{r\alpha}/\mu_\alpha$ with $k_{r\alpha}$ and μ_α being the phase relative permeability and viscosity, respectively, p is the fluid pressure and K is the rock matrix absolute permeability tensor. Besides, $(q_\alpha)_m$ represents source or sink terms (i.e., injection or production wells) for phaseα. Here, ϕ is the porosity of the medium, ρ_α and S_α are, respectively, the density and saturation of phase α, and n_{frac} is the number of fractures within Ω_m. Moreover, $(\varphi_\alpha)_{m,f_k}$ is the phase transfer term between Ω_m and Ω_{f_k} (the k-th fracture intersecting Ω_m), which is defined as Hajibeygi et al. (2011):

$$(\varphi_\alpha)_{m,f_k} = -\rho_\alpha \lambda_\alpha \mathrm{K}_{m,f_k} \frac{\mathcal{J}_C^{m,f_k}}{V_m}\left(p_{f_k} - p_m\right) \tag{2}$$

in which $\mathcal{J}_C^{m,f_k}$ is the connectivity index between Ω_m and Ω_{f_k}. These terms will be adequately addressed in section 3. Similarly, to Eq. (1), considering a domain Ω_{f_k} representing the k-th of these 2-D fractures, for phase α, we can write:

$$\frac{\partial}{\partial t}(\omega\phi\rho_\alpha S_\alpha)_{f_k} + \nabla\cdot\left(\omega\rho_\alpha \vec{v}_\alpha\right)_{f_k} = (\rho_\alpha q_\alpha)_{f_k} + (\rho_\alpha \varphi_\alpha)_{f_k,m} + \sum_{j=1}^{n_{frac}} (\rho_\alpha \varphi_\alpha)_{f_k,f_j;j\neq k} \tag{3}$$

in which $(\omega)_{f_k}$ is the aperture of the fracture Ω_{f_k}, $(q_\alpha)_{f_k}$ is an areal averaged source term of phaseα and $(\varphi_\alpha)_{f_k,m}$ and $(\varphi_\alpha)_{f_k,f_j}$ are areal averaged phase transfer terms analogous to $(\varphi_\alpha)_{m,f_k}$, defined as:

$$(\varphi_\alpha)_{f_k,m} = -\rho_\alpha \lambda_\alpha \mathrm{K}_{m,f_k} \frac{\mathscr{J}_C^{m,f_k}}{A_{f_k}} \left(p_m - p_{f_k}\right) \tag{4}$$

and:

$$(\varphi_\alpha)_{f_k,f_j} = -\rho_\alpha \lambda_\alpha \mathrm{K}_{f_k,f_j} \frac{\mathscr{J}_C^{f_k,f_j}}{A_{f_k}} \left(p_{f_j} - p_{f_k}\right) \tag{5}$$

The appropriate initial and boundary conditions are typically given, by Aziz and Settare (1979); Contreras et al. (2016):

$$\begin{cases} p(\vec{x},t) = g_D & on \quad \Gamma_m^D \times [0,t] \\ \vec{v}\cdot\vec{n} = g_N & on \quad \Gamma_m^N \times [0,t] \\ p(\vec{x},t) = g_{\mathscr{W},1} \ or \int_{\Gamma_{\mathscr{W}}} \vec{v}\cdot\vec{n}\,\partial\Gamma_{\mathscr{W}} = g_{\mathscr{W},2} & on \quad \Gamma_m^{\mathscr{W}} \times [0,t] \\ S_w(\vec{x},0) = \overline{S}_w^0 & on \quad \Omega_m \\ p(\vec{x},0) = \overline{p}^0 & on \quad \Omega_m \end{cases} \tag{6}$$

where Γ_m^D and Γ_m^N are the Dirichlet and Neumann boundaries, respectively, while $\Gamma_m^{\mathscr{W}}$ indicate the wells (with $\mathscr{W} = I, P$ for injector and producer, respectively). Besides, t is the time variable, g_D and $g_{\mathscr{W},1}$ are prescribed scalar functions for the pressure, while g_N and $g_{\mathscr{W},2}$ are prescribed scalar functions for the flux (flow velocity) and flow, respectively. Moreover, $\vec{n}$ is the outward unitary normal vector to the control surface, $\vec{v} = \vec{v}_w + \vec{v}_o$ is the total flow velocity, $\overline{S}_w^0$ and $\overline{p}^0$ are the initial pressure and water saturation distribution throughout the reservoir. Moreover, we consider that all fractures are completely contained in Ω_m, and, therefore, there are no boundary conditions associated to them. Finally, we also consider that the media is fully saturated by oil and water, i.e.:

$$S_w + S_o = 1 \tag{7}$$

3. Numerical formulation

In this section, the numerical scheme used to simulate the two-phase flow of oil and water in fractured reservoirs using general unstructured tetrahedral meshes, arbitrary permeability tensors for the rock matrix and low or high fractures permeabilities, is presented. Consider that Ω_m is discretized by n_{tetra} tetrahedral control-volumes (CVs), so that the i-th one is indexed as $\hat{m}_i$. Also consider that Ω_{f_k} is discretized by ν_{polyg}^k polygonal CVs, so that the j-th one is indexed as $\hat{f}_k^j$. In this context, we integrate Eq. (1) in Ω_m, which is equal to the sum of the integrals of Eq. (1) on the tetrahedral cells $\hat{m}_i$ (with $i = 1 \ldots n_{tetra}$). Considering only the tetrahedron $\hat{m}_i$, applying the Gauss divergence theorem and the mean value theorem, and writing the discrete expression in the residual form, we obtain:

$$\begin{aligned}(r_\alpha)_{\hat{m}_i}^{\tau+1} = {} & V_{\hat{m}_i}(\rho_\alpha q_\alpha)_{\hat{m}_i}^{\tau+1} - \phi_{\hat{m}_i} V_{\hat{m}_i} \frac{(\rho_\alpha S_\alpha)_{\hat{m}_i}^{\tau+1} - (\rho_\alpha S_\alpha)_{\hat{m}_i}^{\tau}}{\Delta t} \\ & - \sum_{j=1}^{n_{tetra}} (\rho_\alpha \mathscr{T}_\alpha)_{\hat{m}_i,\hat{m}_j}^{\tau+1} + \sum_{k=1}^{n_{frac}} \sum_{j=1}^{\nu_{polyg}^k} (\rho_\alpha \mathscr{T}_\alpha)_{\hat{m}_i,\hat{f}_k^j}^{\tau+1}\end{aligned} \tag{8}$$

in which $V_{\hat{m}_i}$ is the volume of $\hat{m}_i$, τ is the time step counter and $(\rho_\alpha \mathscr{T}_\alpha)_{\hat{m}_i,\hat{m}_j}$ is the mass flow rate of the phase α between rock matrix cells $\hat{m}_i$ and $\hat{m}_j$ (which is null if the referred cells are not neighbors), and $\mathscr{T}_\alpha$ is its volumetric flow rate. $(\rho_\alpha \mathscr{T}_\alpha)_{\hat{m}_i,\hat{f}_k^j}$ is the analogous term for a matrix-facture interaction, which is null if the matrix cell $\hat{m}_i$ is not intersected by the fracture cell $\hat{f}_k^j$. We can write a similar expression for $\hat{f}_k^j$, whose area is $A_{\hat{f}_k^j}$, based on Eq. (3), as:

$$\begin{aligned}(r_\alpha)_{\hat{f}_k^j}^{\tau+1} = {} & A_{\hat{f}_k^j}(\rho_\alpha q_\alpha)_{\hat{f}_k^j}^{\tau+1} - \omega_{f_k} \phi_{\hat{f}_k^j} A_{\hat{f}_k^j} \frac{(\rho_\alpha S_\alpha)_{\hat{f}_k^j}^{\tau+1} - (\rho_\alpha S_\alpha)_{\hat{f}_k^j}^{\tau}}{\Delta t} \\ & - \sum_{i=1}^{\nu_{polyg}^k} \omega_{f_k} (\rho_\alpha \mathscr{T}_\alpha)_{\hat{f}_k^j,\hat{f}_k^i}^{\tau+1} - \sum_{i=1}^{n_{tetra}} (\rho_\alpha \mathscr{T}_\alpha)_{\hat{m}_i,\hat{f}_k^j}^{\tau+1} + \sum_{h=1}^{n_{frac}} \sum_{i=1}^{\nu_{polyg}^h} (\rho_\alpha \mathscr{T}_\alpha)_{\hat{f}_k^j,\hat{f}_h^i;\ h\neq k}^{\tau+1}\end{aligned} \tag{9}$$

in which $(\rho_\alpha \mathscr{T}_\alpha)_{\hat{f}_k^j,\hat{f}_k^i}$ is the interaction term for neighboring polygonal cells in the same fracture (Ω_{f_k}) and:

$$(\rho_\alpha \mathscr{T}_\alpha)_{\hat{m}_i,\hat{f}_k^j} = \int_{V_{\hat{m}_i}} (\rho_\alpha \varphi_\alpha)_{m,\hat{f}_k^j} dV_{\hat{m}_i} = -\int_{A_{\hat{f}_k^j}} (\rho_\alpha \varphi_\alpha)_{f_k,\hat{m}_i} dA_{\hat{f}_k^j} = -(\rho_\alpha \mathscr{T}_\alpha)_{\hat{f}_k^j,\hat{m}_i} \tag{10}$$

and the interaction term for polygonal cells in different fractures (intersecting each other) is:

$$(\rho_\alpha \mathscr{T}_\alpha)_{\hat{f}_k^j,\hat{f}_h^i;\ h\neq k} = \int_{A_{\hat{f}_k^j}} (\rho_\alpha \varphi_\alpha)_{f_k,\hat{f}_h^i} dA_{\hat{f}_k^j} = -\int_{A_{\hat{f}_h^i}} (\rho_\alpha \varphi_\alpha)_{f_h,\hat{f}_k^j} dA_{\hat{f}_h^i} = -(\rho_\alpha \mathscr{T}_\alpha)_{\hat{f}_h^i,\hat{f}_k^j} \tag{11}$$

The terms above are detailed in section 3.2. In Eqs. (8) and (9), the source terms $(\rho_\alpha q_\alpha)_{\hat{m}_i}$ and $(\rho_\alpha q_\alpha)_{\hat{f}_k^j}$ are calculated for the wells using the Peaceman model (Peaceman, 1977), in which context, the bottom-hole flow is considered to be proportional to the difference between the bottom-hole pressure and the pressure of the cell containing the well:

$$\begin{cases} (\rho_\alpha q_\alpha)_{\hat{m}_i} = \rho_\alpha \lambda_\alpha \mathrm{K}_{\hat{m}_i} \dfrac{\mathscr{J}_W}{V_{\hat{m}_i}} \left(p_W - p_{\hat{m}_i}\right) \\ (\rho_\alpha q_\alpha)_{\hat{f}_k^j} = \rho_\alpha \lambda_\alpha \mathrm{K}_{\hat{f}_k^j} \dfrac{\mathscr{J}_W}{A_{\hat{f}_k^j}} \left(p_W - p_{\hat{f}_k^j}\right) \end{cases} \tag{12}$$

in which $\mathscr{J}_W$ is the well productivity index, p_W is the bottom-hole pressure, $p_{\hat{m}_i}$ is the pressure at CV $\hat{m}_i$, $p_{\hat{f}_k^j}$ is the pressure at CV $\hat{f}_k^j$.

In the expressions above, ρ_α and λ_α are computed considering the upwind direction. The numerical definition of the phase volumetric flow rates ($\mathscr{T}_\alpha$) are presented in the next subsections.

Writing the Eqs. (9) and (10) for all CVs of the computational mesh, including fractures (polygonal CVs) and matrix blocks (tetrahedral CVs), we get a non-linear system of equations whose solution can be obtained by the Newton-Raphson (NR) method (Chen et al., 2006). Therefore, in each NR iteration (υ) we have:

$$r_\alpha^{\upsilon+1} \approx r_\alpha^{\upsilon} + \left(\frac{\partial r_\alpha}{\partial p}\right)^{\upsilon} \delta p^{\upsilon+1} + \left(\frac{\partial r_\alpha}{\partial S}\right)^{\upsilon} \delta S^{\upsilon+1} \tag{13}$$

in which $r_\alpha = \begin{bmatrix} r_{\alpha,\hat{m}} & r_{\alpha,\hat{f}} \end{bmatrix}^T$ is the vector of the residuals for each degree of freedom in the domains Ω_m and Ω_{f_k} (with $k = 1$ to n_{frac}) and, similarly, $\delta p = \begin{bmatrix} \delta p_{\hat{m}} & \delta p_{\hat{f}} \end{bmatrix}^T$ and $\delta S = \begin{bmatrix} \delta S_{\hat{m}} & \delta S_{\hat{f}} \end{bmatrix}^T$. Then, considering that we have 2 phases (i.e., oil and water), we can find the roots of Eq. (13) by:

$$\begin{bmatrix} r_{1,\hat{m}} \\ r_{1,\hat{f}} \\ r_{2,\hat{m}} \\ r_{2,\hat{f}} \end{bmatrix}^{\upsilon} + \mathscr{J}^{\upsilon} \begin{bmatrix} \delta p_{\hat{m}} \\ \delta p_{\hat{f}} \\ \delta S_{\hat{m}} \\ \delta S_{\hat{f}} \end{bmatrix}^{\upsilon+1} = 0 \rightarrow \begin{bmatrix} \delta p_{\hat{m}} \\ \delta p_{\hat{f}} \\ \delta S_{\hat{m}} \\ \delta S_{\hat{f}} \end{bmatrix}^{\upsilon+1} = -\{\mathscr{J}^{\upsilon}\}^{-1} \begin{bmatrix} r_{1,\hat{m}} \\ r_{1,\hat{f}} \\ r_{2,\hat{m}} \\ r_{2,\hat{f}} \end{bmatrix}^{\upsilon} \tag{14}$$

in which the Jacobian matrix ($\mathscr{J}$) is defined as:

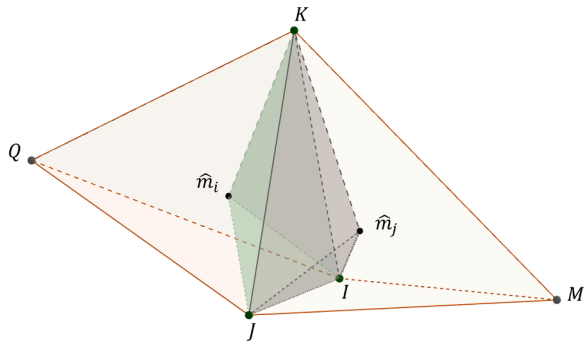

Fig. 1. Face ***IJK*** shared by the tetrahedrons $\hat{L}$ and $\hat{R}$, highlighting MPFA-D stencil. Source: adapted from the work of Cavalcante et al. (2022).

$$\mathscr{J} = \begin{bmatrix} \begin{bmatrix} \mathscr{J}^{mm}_{1p} & \mathscr{J}^{mf}_{1p} \\ \mathscr{J}^{fm}_{1p} & \mathscr{J}^{ff}_{1p} \end{bmatrix} & \begin{bmatrix} \mathscr{J}^{mm}_{1S} & \mathscr{J}^{mf}_{1S} \\ \mathscr{J}^{fm}_{1S} & \mathscr{J}^{ff}_{1S} \end{bmatrix} \\ \begin{bmatrix} \mathscr{J}^{mm}_{2p} & \mathscr{J}^{mf}_{2p} \\ \mathscr{J}^{fm}_{2p} & \mathscr{J}^{ff}_{2p} \end{bmatrix} & \begin{bmatrix} \mathscr{J}^{mm}_{2S} & \mathscr{J}^{mf}_{2S} \\ \mathscr{J}^{fm}_{2S} & \mathscr{J}^{ff}_{2S} \end{bmatrix} \end{bmatrix} \tag{15}$$

The convergence criteria for the iterative process is defined as HosseiniMehr et al. (2022):

$$\left(\frac{\| r_1^{p+1} \|_2}{\| r_1^0 \|_2} < \epsilon_1 \text{ or } \frac{\| r_1^{p+1} \|_2}{\| RHS_1 \|_2} < \epsilon_1\right) \text{and} \left(\frac{\| r_2^{p+1} \|_2}{\| r_2^0 \|_2} < \epsilon_2 \text{ or } \frac{\| r_2^{p+1} \|_2}{\| RHS_2 \|_2} < \epsilon_2\right) \text{and} \left(\frac{\| \delta p \|_2}{\| p \|_2} < \epsilon_p \text{ and } \frac{\| \delta S \|_2}{\| S \|_2} < \epsilon_S\right) \tag{16}$$

in which ε_1, ε_2, ε_p and ε_S are tolerances defined by the user, and $\|S\|_2$ is the L-2 norm of the vector containing the phase saturations, what is analogous for the other terms. Moreover, all the prescribed terms, together with the source terms, over phase α will comprise its "Right-Hand Side" (RHS_α) in equations definitions. Naturally there are other possible controls for this iterative process, the user can, for example, define a maximum number of NR iterations to achieve convergence, after which the iterative process must restart using a smaller time step (usually half of the previous one). It is worth mentioning that the time step determination here is made following the work of Cavalcante et al. (2020), but also considering minimum and maximum limits that can be stated by the user.

The matrix-matrix flux calculation (MPFA-D)

The unique flux expression through a face *IJK* shared by $\hat{m}_i$ and $\hat{m}_j$, considering the configuration shown in Fig. 1, can be written as:

$$(\mathscr{F}_\alpha)_{\hat{m}_i,\hat{m}_j} = \vec{v}_\alpha \cdot \vec{N} = \vec{v}^p_\alpha \cdot \vec{N} + \vec{v}^g_\alpha \cdot \vec{N} \tag{17}$$

in which, according to the Darcy velocity definition, the velocity due to pressure gradient is $\vec{v}^p_\alpha \cdot \vec{N} = -\lambda_\alpha \mathrm{K} \nabla p$ and the velocity due to the gravitational force is $\vec{v}^g_\alpha \cdot \vec{N} = \rho_\alpha \lambda_\alpha \mathrm{K} \vec{\mathscr{g}}$, with $\vec{N}$ being the area normal vector of the face shared by $\hat{m}_i$ and $\hat{m}_j$. From the formulation presented by Lira Filho et al. (2021), which is applicable to diffusion problems on 3D tetrahedral meshes, we can define $\vec{v}^p_\alpha \cdot \vec{N}$ and $\vec{v}^g_\alpha \cdot \vec{N}$ as:

$$\vec{v}^p_\alpha \cdot \vec{N} = -\Re \left[\left(p_{\hat{m}_j} - p_{\hat{m}_i}\right) - \frac{1}{2}\mathfrak{D}_{JK}(p_J - p_I) + \frac{1}{2}\mathfrak{D}_{JI}(p_J - p_K) \right] \tag{18}$$

and:

$$\vec{v}^g_\alpha \cdot \vec{N} = \rho_\alpha \mathscr{g} \Re \left[\left(z_{\hat{m}_j} - z_{\hat{m}_i}\right) - \frac{1}{2}\mathfrak{D}_{JK}(z_J - z_I) + \frac{1}{2}\mathfrak{D}_{JI}(z_J - z_K) \right] \tag{19}$$

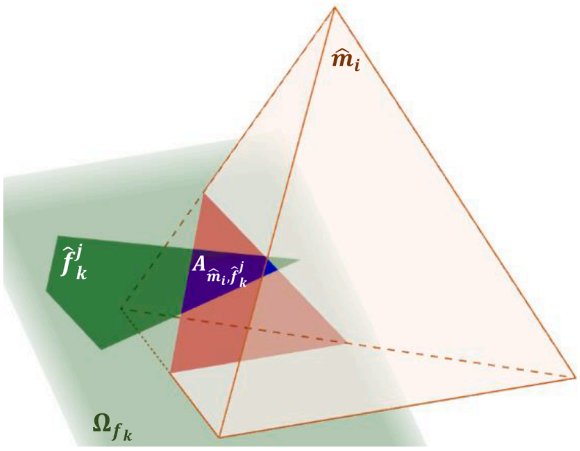

Fig. 2. Intersection between $\hat{m}_i$ and $\hat{f}^j_k$.

with:

$$\Re = \lambda_\alpha \left|\vec{N}\right| \frac{\mathrm{K}^n_{\hat{m}_i} \mathrm{K}^n_{\hat{m}_j}}{h_{\hat{m}_i} \mathrm{K}^n_{\hat{m}_j} + h_{\hat{m}_j} \mathrm{K}^n_{\hat{m}_i}} \tag{20}$$

$$\mathfrak{D}_{ij} = \frac{\left\langle \vec{\tau}_{ij}, \overrightarrow{\hat{L}\hat{R}} \right\rangle}{\left|\vec{N}\right|^2} - \frac{1}{\left|\vec{N}\right|} \left(h_{\hat{m}_i} \frac{\mathrm{K}^{t,ij}_{\hat{m}_i}}{\mathrm{K}^n_{\hat{m}_i}} + h_{\hat{m}_j} \frac{\mathrm{K}^{t,ij}_{\hat{m}_j}}{\mathrm{K}^n_{\hat{m}_j}} \right); \; i,j = I,J,K \tag{21}$$

where:

$$\vec{\tau}_{ij} = \vec{N} \times \vec{ij}; \; \mathrm{K}^n_{\mathscr{k}} = \frac{\vec{N}^T \mathrm{K}_{\mathscr{k}} \vec{N}}{\left|\vec{N}\right|^2}; \; \mathrm{K}^{t,ij}_{\mathscr{k}} = \frac{\vec{N}^T \mathrm{K}_{\mathscr{k}} \vec{\tau}_{ij}}{\left|\vec{N}\right|^2}; \; \mathscr{k} = m_i, m_j; \; i,j = I,J,K \tag{22}$$

in which $h_{\hat{m}_i}$ is the distance (height) of the centroid of $\hat{m}_i$ to the referred face (analogous to $\hat{m}_j$) and λ_α is taken upwind. In this formulation, the auxiliary vertex unknowns (p_I, p_J, p_K) must be interpolated as convex weighted averages of the values of p at the cells sharing the respective node (*I*, *J* or *K*). In this context, we use the least square interpolation strategy presented by Dong and Kang (Dong and Kang, 2021; Dong and Kang, 2022). This scheme approximates the pressure value at a vertex as a combination of its values at the centroids of all the tetrahedral cells sharing that node, returning linearity-preserving explicit weights (LPEW), and has proved to be quite robust when compared with others LPEW interpolations (which could be also applied here) when solving benchmark problems using general unstructured tetrahedral meshes and arbitrary permeability tensors (Cavalcante, 2023). It is worth mentioning that, as other linear MPFAs methods, the MPFA-D scheme is not monotone and for strongly anisotropic permeability tensors or very distorted non-k-orthogonal meshes non monotone solutions may arise. But some relatively simple strategies can be used to remedy this problem (Cavalcante et al., 2022). Moreover, it is also possible to apply other forms of flux approximation than MPFA-D, with due care regarding anisotropy, heterogeneity and meshes.

3.1. The matrix-fracture flux calculation

If a polygonal fracture cell intersects a tetrahedral cell, as shown in Fig. 2, it is necessary to calculate the terms in Eqs. (8) and (9) corresponding to the phase transfer between a tetrahedral cell $\hat{m}_i$ and a polygonal fracture cell $\hat{f}^j_k$. It can be done according to an embedded discrete fracture model adapted to unstructured tetrahedral grids (EDFM-U), based on Eq. (2), and given by:

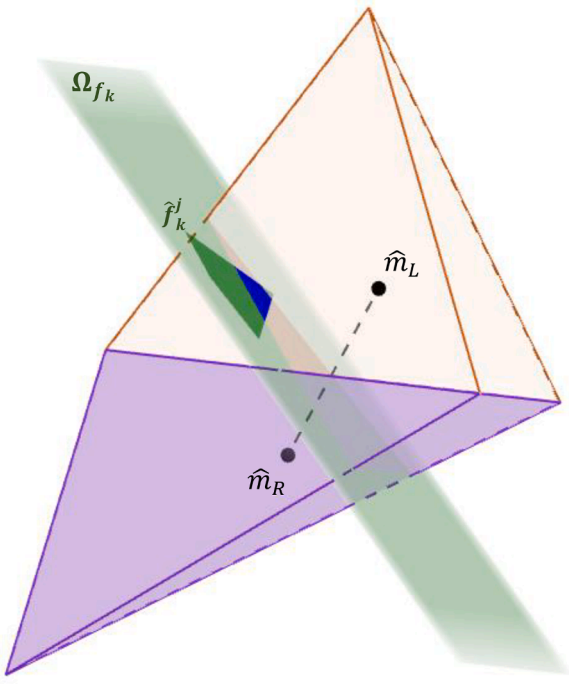

Fig. 3. Intersection between Ω_{f_k} and the segment connecting $\widehat{m}_L$ and $\widehat{m}_R$. The blue region represents the intersection $\widehat{f}_k^j \cap \widehat{m}_L$.

$$(\rho_\alpha \mathcal{T}_\alpha)_{\hat{m}_i \hat{f}_k^j} = -(\rho_\alpha \mathcal{T}_\alpha)_{\hat{f}_k^j, \hat{m}_i} = -\rho_\alpha \lambda_\alpha \mathrm{K}_{\hat{m}_i f_k} \mathcal{I}_C^{\hat{m}_i \hat{f}_k^j} \left(p_{\hat{f}_k^j} - p_{\hat{m}_i}\right) \tag{23}$$

in which ρ_α and λ_α are taken upwind and the connectivity index $\mathcal{I}_C^{\hat{m}_i \hat{f}_k^j}$ is calculated as (HosseiniMehr et al., 2022):

$$\mathcal{I}_C^{\hat{m}_i \hat{f}_k^j} = \frac{A_{\hat{m}_i \hat{f}_k^j}}{\left\langle d_{\hat{m}_i, \hat{m}_i \cap \hat{f}_k^j} \right\rangle} \tag{24}$$

and $\mathrm{K}_{\hat{m}_i f_k}$ is calculated as:

$$\mathrm{K}_{\hat{m}_i f_k} = \frac{(l_{\hat{m}_i} + \omega_{f_k}) \mathrm{K}_{\hat{m}_i}^n K_{f_k}}{\mathrm{K}_{\hat{m}_i}^n \omega_{f_k} + K_{f_k} l_{\hat{m}_i}} \tag{25}$$

where $l_{\hat{m}_i} = \sqrt[3]{V_{\hat{m}_i}}$, ω_{f_k} is the aperture of the fracture Ω_{f_k}, K_{f_k} is the permeability tensor of Ω_{f_k}, with $\mathrm{K}_{f_k} = K_{f_k} \boldsymbol{I}_{3\times 3}$, with $\boldsymbol{I}_{3\times 3}$ being the identity matrix, $\mathrm{K}_{\hat{m}_i}^n$ is defined analogously to Eq. (22), but considering the normal vector to the plane containing $\widehat{f}_k^j$. Moreover, $A_{\hat{m}_i \hat{f}_k^j}$ is the area of $\hat{m}_i \cap \widehat{f}_k^j$ (whose calculation is presented in detail in the work of Cavalcante (2023) and $\langle d_{\hat{m}_i, \hat{m}_i \cap \hat{f}_k^j} \rangle$ is the average distance between $\hat{m}_i$ and $\hat{m}_i \cap \widehat{f}_k^j$, calculated as:

$$\left\langle d_{\hat{m}_i, \hat{m}_i \cap \hat{f}_k^j} \right\rangle = \frac{1}{V_{\hat{m}_i}} \int_{V_{\hat{m}_i}} \left| \vec{r}_{\hat{m}_i \cap \hat{f}_k^j, \hat{m}_i} \cdot \vec{n}_{\hat{f}_k} \right| dV_{\hat{m}_i} \tag{26}$$

in which $\vec{r}_{\hat{m}_i \cap \hat{f}_k^j, \hat{m}_i}$ is a vector from the centroid of $\hat{m}_i \cap \widehat{f}_k^j$ to a point in $\hat{m}_i$ and $\vec{n}_{\hat{f}_k}$ is the unitary normal vector to Ω_{f_k}. It is important to stablish that, when determining $A_{\hat{m}_i \hat{f}_k^j}$, if one or two vertices of $\hat{m}_i$ are on Ω_{f_k}, $A_{\hat{m}_i \hat{f}_k^j} = 0$. If three vertices of $\hat{m}_i$ are on Ω_{f_k}, the area of $\hat{m}_i \cap \Omega_{f_k}$ is that of the face comprised by these vertices. More than this, if one or two vertices of $\widehat{f}_k^j$ are on a face of $\hat{m}_i$, similarly, $A_{\hat{m}_i \hat{f}_k^j} = 0$, and, if all the vertices of $\widehat{f}_k^j$ are on the same face of $\hat{m}_i$, then $A_{\hat{m}_i \hat{f}_k^j}$ is the area of the polygon $\widehat{f}_k^j$. Naturally, the determination of if a vertex is or not on the planes is made considering a tolerance (Cavalcante, 2023).

These procedures are insufficient to reproduce the effects of low permeability fractures in the flow simulation since the EDFM-U matrix-fracture interaction term, given by Eqs. (23) to (26) will be as low as the permeability of the fracture. Therefore, the presence of low permeability fractures makes little difference in the model. Besides, EDFM-U does not include any modification in matrix-matrix interaction, which prevents it from reproducing the effect of blocking the flow between two matrix cells due to the existence of a low permeability fracture. In this context, a projection-based embedded discrete fracture model adapted to unstructured tetrahedral grids (pEDFM-U) considers that the fractures may also modify the matrix-matrix fluxes. In this work, we admit that, if a fracture Ω_{f_k} intersects the segment connecting the centroids of two tetrahedra $\hat{m}_L$ and $\hat{m}_R$ sharing a face, as shown in Fig. 3, the matrix-matrix interactions between them, calculated according to Eq. (17) is cancelled (HosseiniMehr et al., 2022).

Moreover, in the pEDFM-U, we consider additional matrix-fracture interactions under the same conditions. Considering the situation shown in Fig. 4, showing pEDFM projections in a 2-D cartesian grid for didactic purposes, the fracture Ω_{f_k} intersects the segment connecting the centroids $\hat{m}_L$ and $\hat{m}_R$, sharing a face $\overline{F}$. This way, the intersections between the fracture cells within Ω_{f_k} (e.g., $\widehat{f}_k^j$ and $\widehat{f}_k^x$) and $\hat{m}_L$ must be

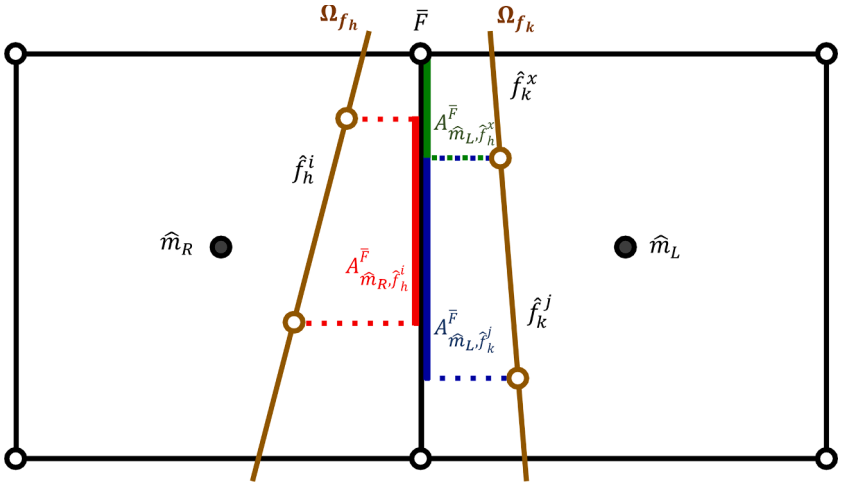

Fig. 4. pEDFM fractures projections.

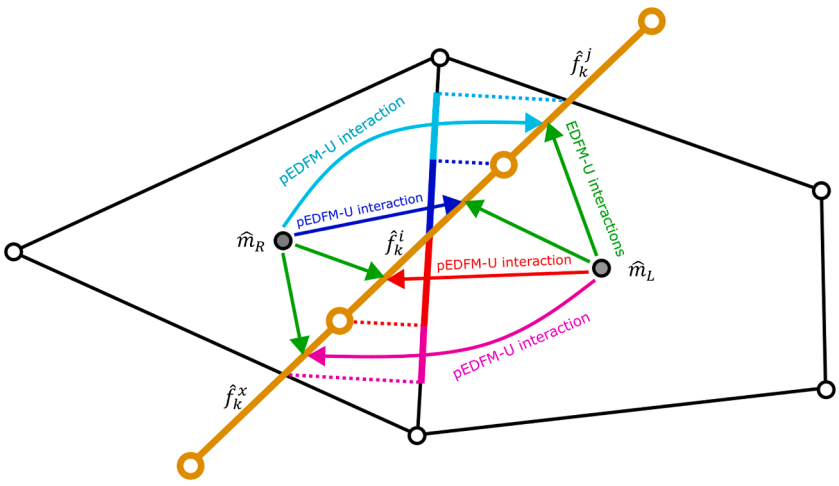

Fig. 5. Summary of matrix-fracture interactions.

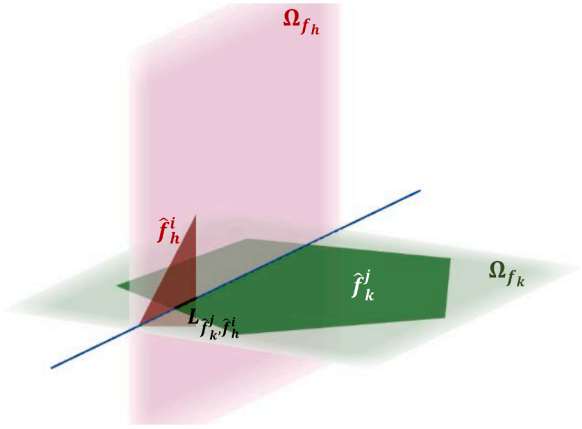

Fig. 6. Intersection between $\widehat{f}_h^i$ and $\widehat{f}_k^j$.

projected on $\overline{F}$ and, through these projections, $\widehat{f}_k^j$ and $\widehat{f}_k^x$ should interact with $\hat{m}_R$. Considering the cell $\widehat{f}_k^j$, the additional pEDFM-U interaction between it and $\hat{m}_R$ can be calculated as:

$$(\rho_\alpha \mathscr{T}_\alpha)_{\hat{m}_R \widehat{f}_k^j} = -(\rho_\alpha \mathscr{T}_\alpha)_{\widehat{f}_k^j \hat{m}_R} = -\rho_\alpha \lambda_\alpha \mathrm{K}^{\overline{F}}_{\hat{m}_R f_k} \mathscr{I}^{\hat{m}_R \widehat{f}_k^j}_{C,\overline{F}} \left(p_{\widehat{f}_k^j} - p_{\hat{m}_R}\right) \tag{27}$$

with:

$$\mathrm{K}^{\overline{F}}_{\hat{m}_R f_k} = \frac{(\omega_{f_k} + l_{\hat{m}_R}) \mathrm{K}^n_{\hat{m}_R} K_{f_k}}{\mathrm{K}^n_{\hat{m}_R} \omega_{f_k} + K_{f_k} l_{\hat{m}_R}} \tag{28}$$

in which $\mathrm{K}^n_{\hat{m}_R}$ is calculated considering Eq. (22) and the unitary normal vector to $\overline{F}$. Besides:

$$\mathscr{I}^{\hat{m}_R \widehat{f}_k^j}_{C,\overline{F}} = \frac{A^{\overline{F}}_{\hat{m}_L \widehat{f}_k^j}}{\left\langle d_{\hat{m}_R, \hat{m}_L \cap \widehat{f}_k^j} \right\rangle} \tag{29}$$

This additional pEDFM-U interaction needs to be added with the previously presented EDFM-U one, shown in Eq. (23). Fig. 5 summarizes the matrix-fracture interactions considered in this work. In this figure, there is again a fracture Ω_{f_k} intersecting the segment connecting the centroids $\hat{m}_L$ and $\hat{m}_R$. The fracture cell $\widehat{f}_k^i$, for example, intersects $\hat{m}_L$ and, as a consequence, it has an EDFM-U interaction with it, to be calculated according to Eq. (23). Additionally, $\widehat{f}_k^i$ also intersects $\hat{m}_R$. Because of this, the part of $\widehat{f}_k^i$ which is inside $\hat{m}_R$ has a pEDFM-U interaction with $\hat{m}_L$, to be calculated according to Eq. (27). Also, the part of $\widehat{f}_k^j$ within $\hat{m}_L$ has an EDFM-U interaction with $\hat{m}_L$ and a pEDFM-U interaction with $\hat{m}_R$.

3.2. The fracture-fracture flux calculation

The terms in Eq. (9) corresponding to the phase transfer between two polygonal CVs ($\widehat{f}_k^i$ and $\widehat{f}_k^j$) contained in the same fracture Ω_{f_k} are calculated as:

$$(\rho_\alpha \mathscr{T}_\alpha)_{\widehat{f}_k^j \widehat{f}_k^i} = -(\rho_\alpha \mathscr{T}_\alpha)_{\widehat{f}_k^i \widehat{f}_k^j} = -\rho_\alpha \lambda_\alpha \mathrm{K}_{f_k} \omega_{f_k} \frac{L_{\widehat{f}_k^j \widehat{f}_k^i}}{d_{\widehat{f}_k^j \widehat{f}_k^i}} \left(p_{\widehat{f}_k^j} - p_{\widehat{f}_k^i}\right) \tag{30}$$

in which $L_{\widehat{f}_k^j \widehat{f}_k^i}$ is the length of the edge shared by $\widehat{f}_k^i$ and $\widehat{f}_k^j$ and $d_{\widehat{f}_k^j \widehat{f}_k^i}$ is the distance between their centroids.

On the other hand, if two polygonal CVs ($\widehat{f}_h^i$ and $\widehat{f}_k^j$) contained in different fractures Ω_{f_h} and Ω_{f_k} intersect each other, as shown in Fig. 6, it is necessary to calculate the phase transfer term between them, by:

$$(\rho_\alpha q_\alpha)_{\widehat{f}_k^j \widehat{f}_h^i} = -(\rho_\alpha q_\alpha)_{\widehat{f}_h^i \widehat{f}_k^j} = -\rho_\alpha \lambda_\alpha \mathrm{K}_{f_k f_h} \zeta_{\widehat{f}_k^j \widehat{f}_h^i} \left(p_{\widehat{f}_h^i} - p_{\widehat{f}_k^i}\right) \tag{31}$$

in which $\mathrm{K}_{f_k f_h}$ is defined as:

$$\mathrm{K}_{f_k f_h} = \frac{(\omega_{f_k} + \omega_{f_h}) K_{f_k} K_{f_h}}{K_{f_h} \omega_{f_k} + K_{f_k} \omega_{f_h}} \tag{32}$$

and $\zeta_{\widehat{f}_k^j \widehat{f}_h^i}$ is given by:

$$\zeta_{\widehat{f}_k^j \widehat{f}_h^i} = \frac{(\omega_{f_k} + \omega_{f_h}) L_{\widehat{f}_k^j \widehat{f}_h^i}}{\left\langle d_{\widehat{f}_k^j \widehat{f}_h^i} \right\rangle + \left\langle d_{\widehat{f}_h^i \widehat{f}_k^j} \right\rangle} \tag{33}$$

Again, in both cases, ρ_α and λ_α are computed by an upwind approximation.

4. Results

In this section, we present some results involving the numerical simulation of single-phase flow and immiscible two-phase flow of oil and water in heterogeneous, anisotropic and fractured porous media. They are all 3D example in which the subdomains containing fractures (Ω_{f_i}) are represented by 2D rectangles discretized using structured quadrilateral grids.

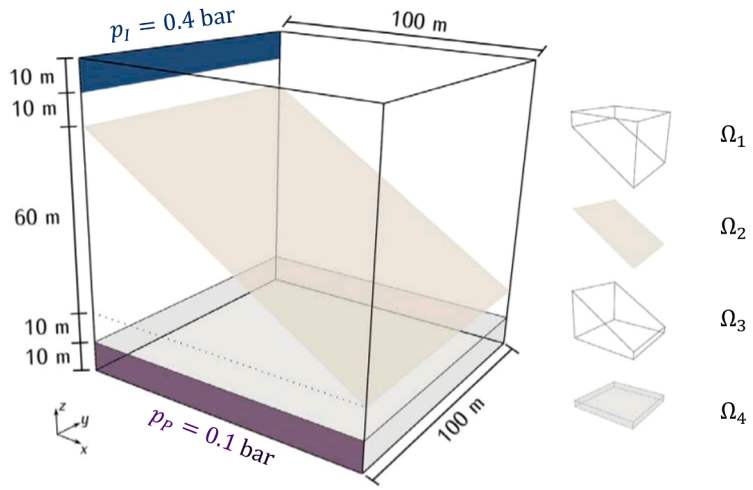

Fig. 7. Domain for test 4.1 - Single-Phase Flow in a Domain Divided into Four Parts. Adapted from Berre et al. (2021).

Table 1
Results for test 4.1 - Single-Phase Flow in a Domain Divided into Four Parts.

n_{tetra}	$\mathscr{E}_p^2$	$\mathscr{R}_p$
9,919	0.0299	–
39,705	0.0232	0.5497
161,303	0.0165	0.7274
531,961	0.0103	1.1853

We have five examples, of which the first three present some quantitative analysis (sections 4.1 to 4.3), while the last two ones present some qualitative evaluation of the capability of our pEDFM-U to deal with full permeability tensors (section 4.4) and high heterogeneity (section 4.5). The quantitative evaluations are made against some reference result, got from other author or manufactured by us using Cartesian (structured) grids, Two Point Flux Approximation (TPFA) and the classical pEDFM (Tene et al., 2017) to handle fractures.

For all the two-phase flow problems presented, the relatives permeabilities are calculated by simple linear relations, given by: $k_{rw} = S_w$ and $k_{ro} = 1 - S_w$. Besides, unless stated otherwise, rock properties are established and fluid properties are approximated as: $\phi = 0.2$ (rock porosity), $\rho_w = 1000$ kg/m^2 (water density), $\rho_o = 800$ kg/m^3 (oil density), $\mu_w = 0.001$Pa $\cdot$ s (water viscosity), $\mu_o = 0.001$Pa $\cdot$ s (oil viscosity), $S_w^0 = 0$ (initial water saturation), $S_o^0 = 1$ (initial oil saturation), $p_w^0 = p_o^0 = 0.2$GPa (initial phase pressure), while $\boldsymbol{I}$ is the identity matrix. Furthermore, in all simulations, $\omega_{f_k} = 0.005$ m with $k = 1 \ldots n_{frac}$. It is worth mentioning that we did not test higher properties differences between phases, as in the case of existing gas, because our model does not consider the possibility of gas being dissolved in liquid phases.

Furthermore, in terms of simulation settings, we adopted $\varepsilon_1 = \varepsilon_2 = \varepsilon_p = \varepsilon_S = 10^{-4}$ to be used in convergence checking presented in Eq. (16), the maximum number of NR iterations to convergence as 5 and the minimum and maximum limits for time step as 0.1 and 30 days, respectively.

4.1. Single-Phase flow in a domain divided into four parts

This example was included to demonstrate the capability of the methodology proposed here to accurately reproduce the pressure field in context of a fractured reservoir. It is based on the benchmark test case 1 of Berre et al. (2021) with a domain $\Omega_m = [0, 100]^3$ m divided into four subdomains $\Omega_m = \cup_{i=1}^4 \Omega_i$ according to Fig. 7.

In Fig. 7, Ω_2 is a planar fracture with an aperture of 0.01 m. The rock matrix domains Ω_1 and Ω_3 are, respectively, the subdomains above and below to Ω_2. The subdomain Ω_4 represents a heterogeneity within the rock matrix. There are two parts of the cube faces that are assigned as Dirichlet boundaries. One has prescribed pressure of $p_I = 0.4$ bar and is marked in blue in Fig. 7, while the other has prescribed pressure of $p_P = 0.1$ bar and is marked in purple in Fig. 7. All remaining parts of the boundary are assigned no flow conditions. Moreover, the permeability tensors are defined as:

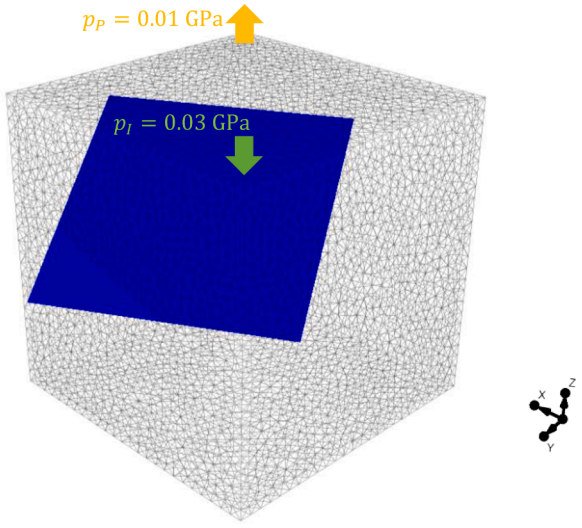

Fig. 8. Domain configuration for test 4.2 - Flow in an Isotropic Media in a Cuboid Reservoir with One Fracture.

$$\mathrm{K}_i = \kappa_i \boldsymbol{I}_{3\times 3} \text{ in } \Omega_i \text{ with } (i = 1 \ldots 4) \tag{34}$$

with $\kappa_1 = \kappa_3 = 10^{-6}$ D (darcy), $\kappa_2 = 10^{-3}$ D and $\kappa_4 = 10^{-5}$ D. Beyond this, $\boldsymbol{I}_{3\times 3}$ is the identity matrix. Finally, the porosities are defined as $\phi_1 = \phi_3 = 0.2$, $\phi_3 = 0.25$ and $\phi_4 = 0.4$.

Four unstructured tetrahedral meshes were used, in this example, to obtain the pressure field, respectively with 9919; 39,705; 161,303 and 531,961 cells. The reference solution was obtained from the work of Gläser (2020). Table 1 presents the results of this test, in terms of L-2 error ($\mathscr{E}_p^2$) and convergence ratio ($\mathscr{R}_p$), both calculated in the same way than in the work of Cavalcante et al. (2022). In this table, n_{tetra} is the number of tetrahedral cells and, as expected, the response obtained from the finest grid is the closest one to the reference solution. Note that the

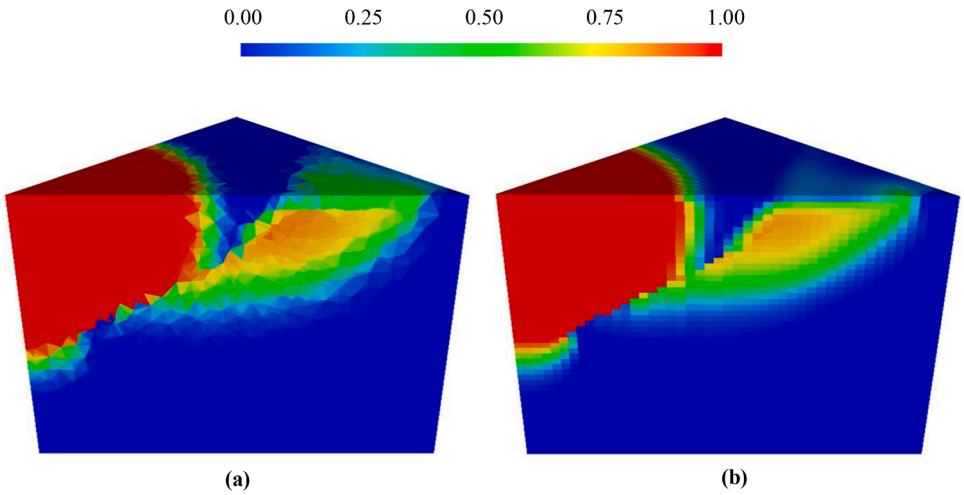

Fig. 9. Water saturation field, after 750 days, for test 4.2.1 - Case 1 – Conductive Fracture. Slice by a parallel plane to axis z and crossing both wells. (a) Tetrahedral grid with 60,963 CVs. (b) Structured cartesian grid with 103,823 CVs.

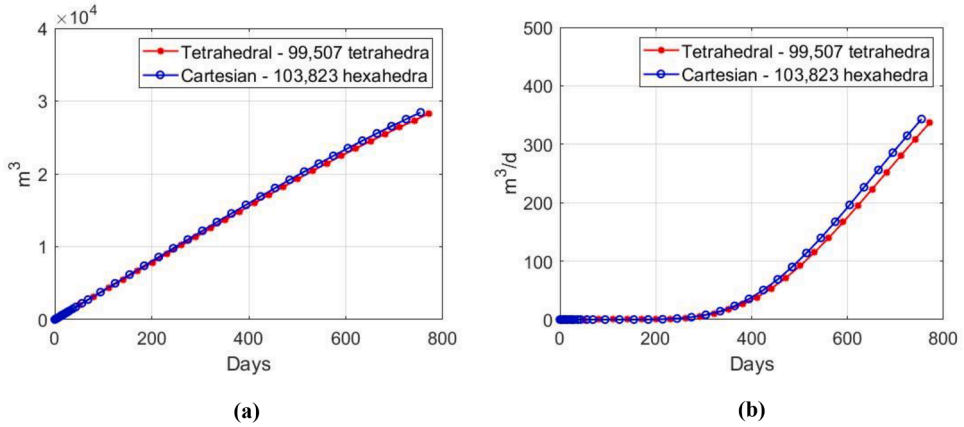

Fig. 10. Cumulative oil and water production of test 4.2.1 - Case 1 – Conductive Fracture. (a) Cumulative oil production. (b) Watercut.

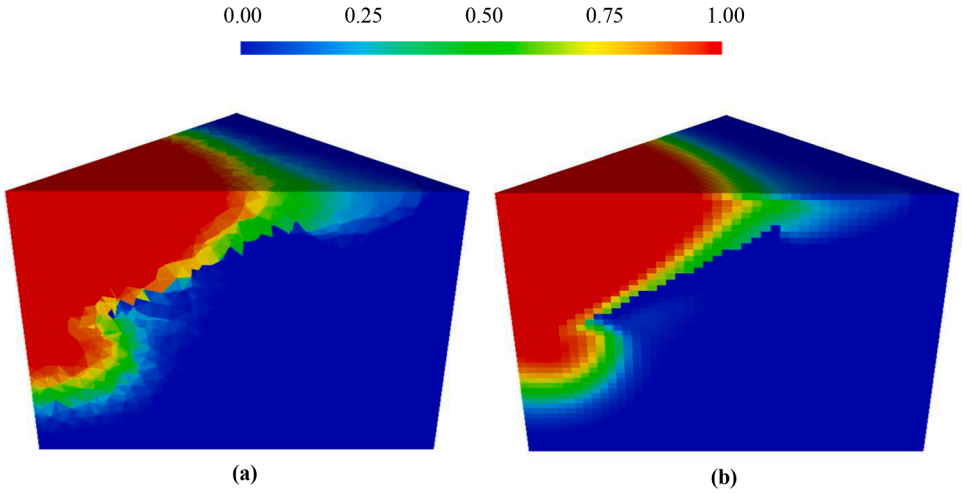

Fig. 11. Water saturation field, after 770 days, for test 4.2.2 - Case 2 – Flow Barrier. Slice by a parallel plane to axis z and crossing both wells. (a) Tetrahedral grid with 60,963 CVs. (b) Structured cartesian grid with 103,823 CVs.

L-2 errors decreases as the number of degrees of freedom increases, with a crescent convergence ratio, which is a good indication in this type of study.

4.2. Flow in an isotropic media in a cuboid reservoir with one fracture

In the first two-phase flow problem, we consider a cubic domain $\Omega_m = [0, 100]^3$ m with null flux at all its boundaries (closed box). There are

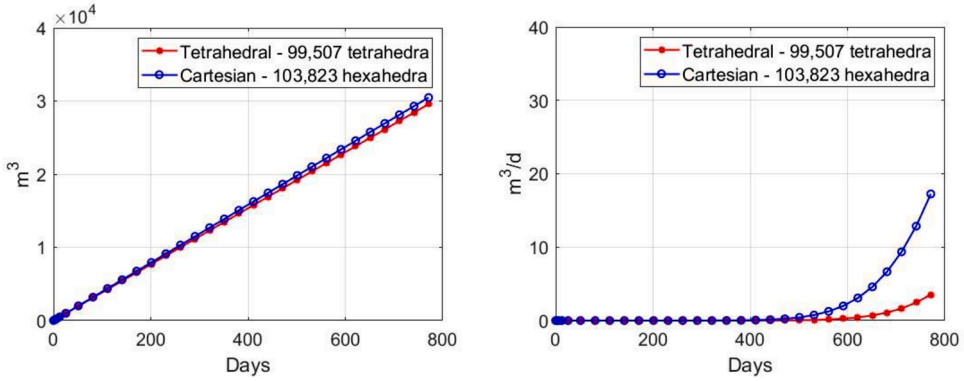

Fig. 12. Cumulative oil and water production of test 4.2.2 - Case 2 – Flow Barrier. (a) Cumulative oil production. (b) Watercut. Note, at ordinate axis, that the magnitude order of the production of water is very low, when compared with the oil production.

two wells: the injector is located at $\vec{x}_I = (10,\ 90,\ 100)$m and we apply a prescribed pressure of $p_I = 0.03$GPa, while the producer is located at $\vec{x}_P = (90,\ 10,\ 100)$m and has a prescribed pressure of $p_P = 0.01$GPa. The compressibility factors of the fluids are defined, respectively, by: $c_{fw} = 0.4 \cdot 10^{-9}\text{Pa}^{-1}$ (water) and $c_{fo} = 0.6 \cdot 10^{-9}\text{Pa}^{-1}$ (oil). The rock matrix permeability is $\text{K}_{\boldsymbol{m}} = \boldsymbol{I}_{3\times 3}\cdot 10^{-14}$ m^2. Moreover, within this domain, there is one fracture and two wells, placed as shown in Fig. 8. We have used a tetrahedral meshes with 60,963 and 99,507 CVs in our scheme. We have compared the pEDFM-U results with those obtained using a structured (cartesian) grid (47 × 47 × 47) with 103,823 CVs, using the classical pEDFM.

The fracture was discretized as a 2D 38 × 38 structured quadrilateral grid and we have considered two different scenarios with two different permeability of the fractures: Case 1 – in which $\text{K}_{f_1} = \boldsymbol{I}_{3\times 3}\cdot 10^{-6}$ m^2 (Conductive Fracture) and Case 2 – in which $\text{K}_{f_2} = \boldsymbol{I}_{3\times 3}\cdot 10^{-22}$ m^2 (Flow Barrier).

4.2.1. Case 1 – conductive fracture

In the first case, we consider a conductive fracture for which the permeability is $\text{K}_{f_1} = \boldsymbol{I}_{3\times 3}\cdot 10^{-6}$ m^2, the results obtained are those shown in Fig. 9 and Fig. 10. Fig. 9 shows the water saturation field after 750 days using a tetrahedral mesh with 60,963 CVs (Fig. 9a) and a structured cartesian mesh with 103,823 CVs (Fig. 9b). These figures present slices in the solutions made by a plane parallel to the z axis and which crosses both wells.

Fig. 9 shows that even the result obtained using the coarsest tetrahedral mesh applied in this example (60,963 cells) clearly indicates the effect of the presence of the high permeability fracture, which quickly leads the water saturation front to the vicinity of the production well. Fig. 10 presents the cumulative oil productions (Fig. 10a) and watercut curves (Fig. 10b) obtained using the tetrahedral mesh with 99,507 cells and the already referred cartesian mesh. The results of oil production and watercut (and water breakthrough) from both meshes are almost coincident, which is a good indication of our pEDFM-U, when compared to another method (pEDFM) which is already established in the literature. Note that both methods indicate a total cumulative oil production around to 28,000 m^3 and that the water breakthrough occurs in about 300 days. It is worth noting that, unlike the simulations using Cartesian mesh or tetrahedral mesh with 60,963 CVs (completed at 750 days), the simulation carried out with the most refined tetrahedral mesh was completed at 770 days.

4.2.2. Case 2 – flow barrier

In Case 2, we consider that the fracture permeability is $\text{K}_{f_1} = \boldsymbol{I}_{3\times 3}\cdot 10^{-22}$ m^2, and the results obtained are those shown in Fig. 11 and Fig. 12. Fig. 11 shows the water saturation field after 770 days using the same tetrahedral mesh used in Case 1 with 60,963 CVs (Fig. 11a) and the structured Cartesian mesh with 103,823 CVs (Fig. 11b).

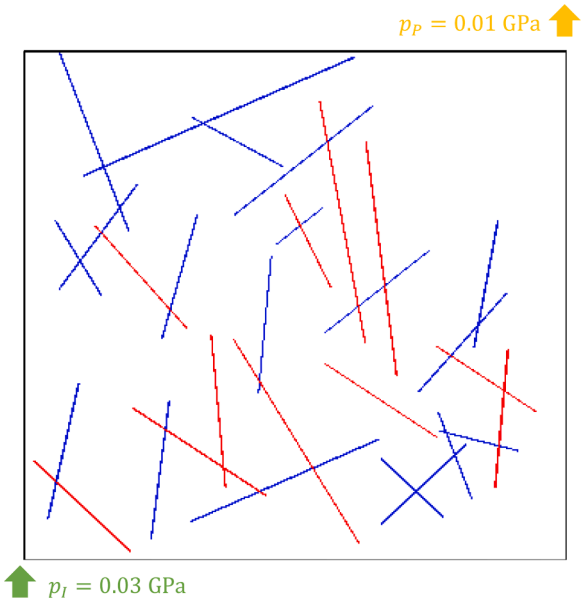

Fig. 13. 2D top visualization of the fractures distribution for the test 4.3 - Flow in an Isotropic Media in a Flat Cuboid Domain with Multiple Fractures.

Fig. 11 shows that again even the result obtained using the coarsest tetrahedral mesh applied in this example (60,963 cells) clearly indicates the effect of the presence of the fracture, which, in this case, is a flow barrier that forces the water saturation front to displaces around it. Fig. 12 presents the cumulative oil productions (Fig. 12a) and watercut curves (Fig. 12b) obtained using the tetrahedral mesh with 99,507 cells and the already referred cartesian mesh. The results of cumulative oil production from both meshes are again almost coincident (indicating about 30,000 m^3 after 770 days), while the watercut ones seems not to be. However, we can conclude that it is a wrong impression just looking at the ordinate axis, since the magnitude order of the production of water is very low, when compared with the oil production, for example (around 1200 m^3/d). In fact, both strategies (pEDFM and pEDFM-U) indicate that there is not a relevant production of water after 770 days.

4.3. Flow in an isotropic media in a flat cuboid domain with multiple fractures

This example is adapted from the work of HosseiniMehr et al. (2022).

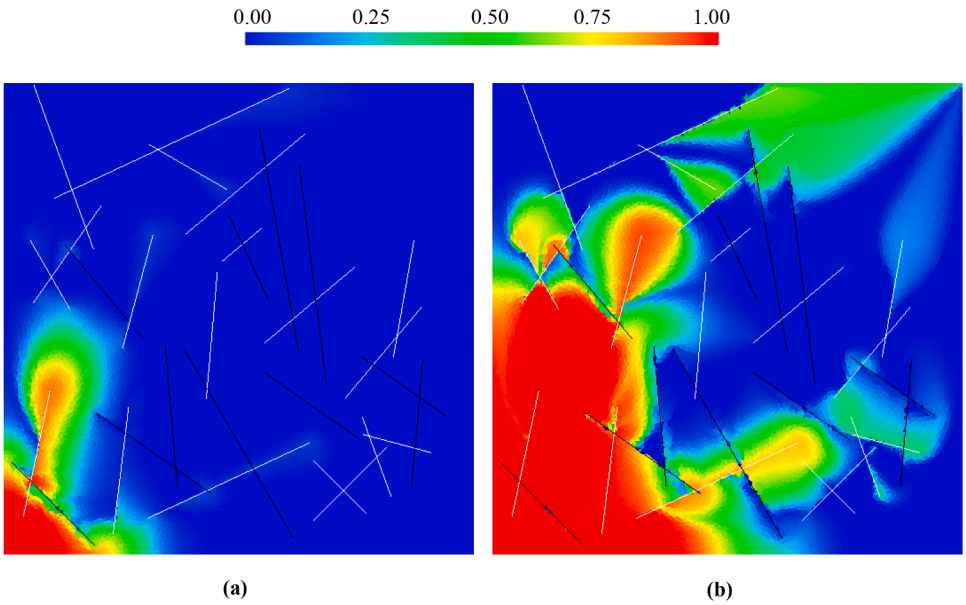

Fig. 14. Results obtained with the pEDFM-U for test 4.3 - Flow in an Isotropic Media in a Flat Cuboid Domain with Multiple Fractures. Conductive fractures are represented by the white lines and barriers by the black lines. Water saturation fields at: (a) 51 days. (b) 291 days.

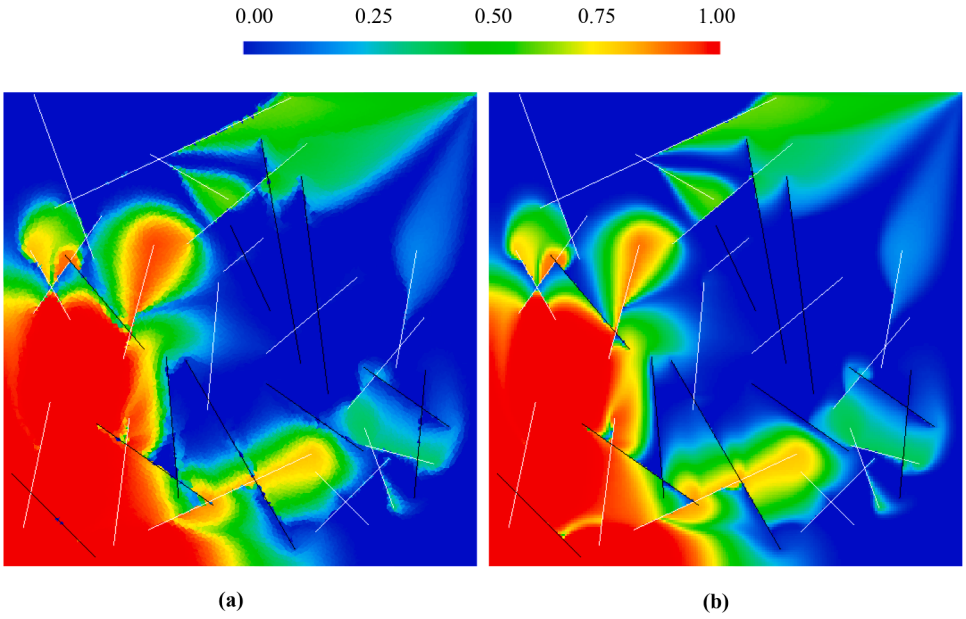

Fig. 15. Results of the test 4.3 - Flow in an Isotropic Media in a Flat Cuboid Domain with Multiple Fractures. fractures are represented by the white lines and barriers by the black lines. Water saturation field at 291 days using: (a) Tetrahedral mesh with 81,455 CVs. (b) Structured (cartesian) grid with 84,872 hexahedral CVs.

In this case, we consider a flat cuboid domain ($\Omega_m = [100 \times 100 \times 1]$ m) with two wells: the injector one at $\vec{x}_I = (0,\ 0,\ 1)$ m have a prescribed pressure $p_I = 0.03$GPa, while the producer one at $\vec{x}_P = (100,\ 100,\ 1)$ m have a prescribed pressure $p_P = 0.01$GPa. Besides, there are 30 fractures distributed as shown in Fig. 13 (blue lines are conductive fractures and red lines are barriers).

The fluids are incompressible and can not cross through the external boundaries of the domain (closed box). Since the depth of the considered domain is very small, in this example, we neglected the gravitational effects. The rock matrix permeability (K_m) and the fractures permeabilities (K_{f1} and K_{f2}) are defined by $K_m = \boldsymbol{I}_{3\times 3}.10^{-14}$ m^2; $K_{f1} = \boldsymbol{I}_{3\times 3}.10^{-6}$ m^2; $K_{f2} = \boldsymbol{I}_{3\times 3}.10^{-22}$ m^2.

Moreover, in this case we use a tetrahedral mesh with 81,455 CVs and each fracture is discretized as a 2D structured grid (40×1), so that $n^k_{polyg} = 40$ with $k = 1 \ldots 30$. Fig. 14 presents the water saturation field obtained using the referred tetrahedral mesh after 51 and 291 days of injection of water. It is possible to observe that the barriers, i.e., the low permeability fractures, marked as black lines, really prevent the advance of the water saturation front through them, forcing it to walk around the barriers. On the other hand, the channels, i.e., the high permeability fractures, marked as white lines, work as fluid conduits in the reservoir, as clearly shown in Figs. 13a and 13b.

Fig. 15 presents the comparison between the water saturation fields obtained by using the tetrahedral mesh (pEDFM-U) with 81,455 CVs and the structured (cartesian) grid (pEDFM) with $206 \times 206 \times 2$ (84,872) hexahedral CVs.

Fig. 15 shows that the results for both approaches are quite similar, demonstrating the capability of our method to reproduce the results

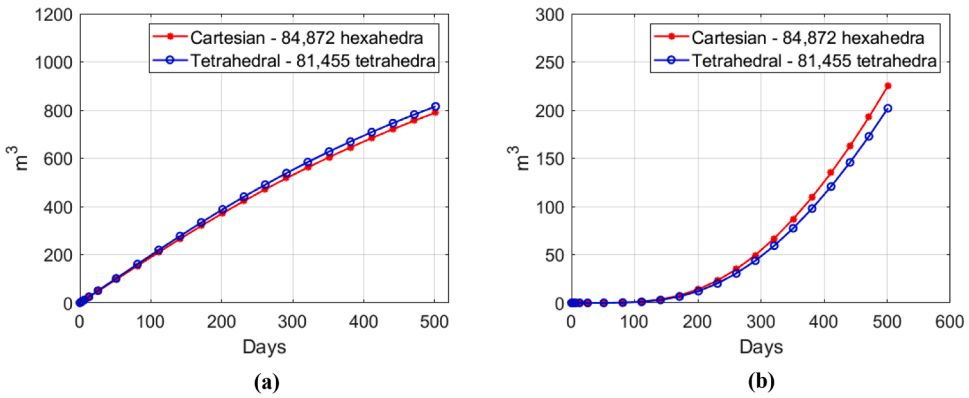

Fig. 16. Cumulative oil and water production for test 4.3 - Flow in an Isotropic Media in a Flat Cuboid Domain with Multiple Fractures. (a) Cumulative oil production. (b) Cumulative water production.

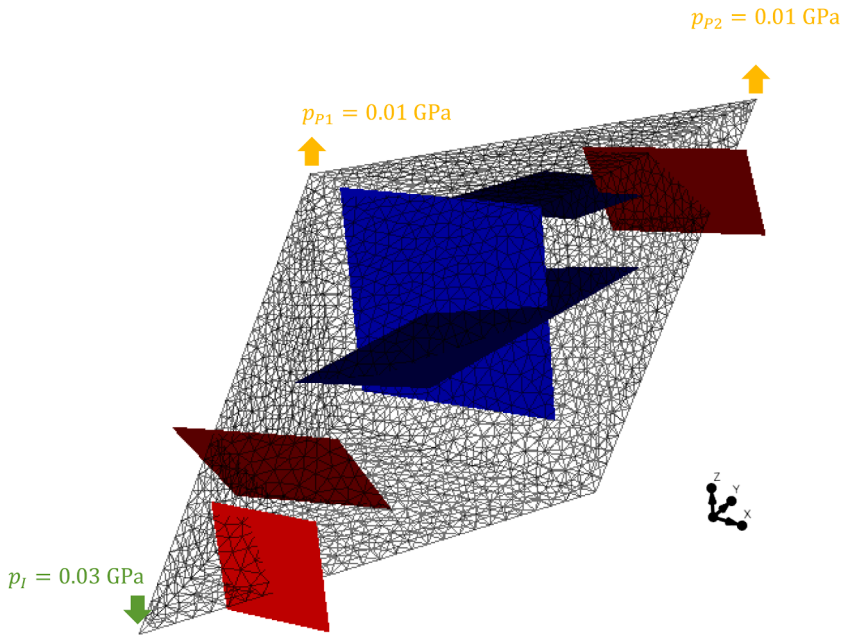

Fig. 17. Domain and fractures and wells positions for test 4.4 - Flow in a Fractured Porous Media with a Full Tensor for the Rock Matrix Permeability in a Non-Cuboid Reservoir. The red rectangles represent low permeabilities fractures, while the blue ones represent high permeabilities fractures.

obtained with other strategy already established in literature. This is reinforced by Fig. 16, which presents the comparison between the solutions obtained with the tetrahedral and the structured grids, in terms of cumulative oil and water production. For both methodologies and meshes, the water breakthroughs are almost simultaneous (see Fig. 16b) and we have approximately 800 m^3 of cumulative oil production after 500 days (see Fig. 16a).

4.4. Flow in a fractured porous media with a full tensor for the rock matrix permeability in a non-cuboid reservoir

In this case, we consider the domain shown in Fig. 17 with a full tensor for the rock matrix permeability (K_m) defined in Eq. (35).

$$K_m = \begin{bmatrix} 0.4219 & 0.2864 & 0.2545 \\ 0.2864 & 0.5594 & 0.2862 \\ 0.2545 & 0.2862 & 0.3187 \end{bmatrix} \cdot 10^{-13} \text{ m}^2 \tag{35}$$

Also, there are three wells, one injector well at $\vec{x}_I = (25,\ 0,\ 0)$ m with a prescribed pressure $p_I = 0.03$GPa and two producer wells at $\vec{x}_{P_1} = (0,\ 75,\ 50)$ m and at $\vec{x}_{P_2} = (50,\ 150,\ 50)$ m with prescribed pressures $p_{P1} = p_{P2} = 0.01$GPa. Besides, there are 6 fractures distributed as shown in Fig. 17. The fractures were discretized as a 2D structured grid with 1.25 m sided squares and placed as shown in Fig. 17, in which the blue ones are the conductive fractures and the red ones are the flow barriers, whose permeabilities are given by $K_{f_1} = \boldsymbol{I}_{3\times 3}.10^{-6}$ m^2 and $K_{f_2} = \boldsymbol{I}_{3\times 3}.10^{-22}$ m^2.

Besides, the fluids are incompressible and can not cross through the boundaries of the domain. Finally, we use an unstructured grid with 22,483 tetrahedral CVs. Fig. 18 shows the water saturation fields in two situations: considering and not considering the presence of the fractures.

Fig. 18a and 17c show the water saturation fields for the case where fractures are not considered, respectively after 231 and 500 days, and we can see the behavior of the fluid flow due to the anisotropic permeability tensor presented in Eq. (35). Fig. 18b shows that when we consider the fracture acting as barrier (fract. on) close to the injection well, marked in black, the flow pattern is completely changed if compared to the fluid flow when we disregard the fractures (fract. off) as it can be seen in Fig. 18a. In the former case, the necessity of circumvent the fracture that acts as a barrier, initially delay the passage of fluid throughout the reservoir. However, later on, when the fluid reaches the

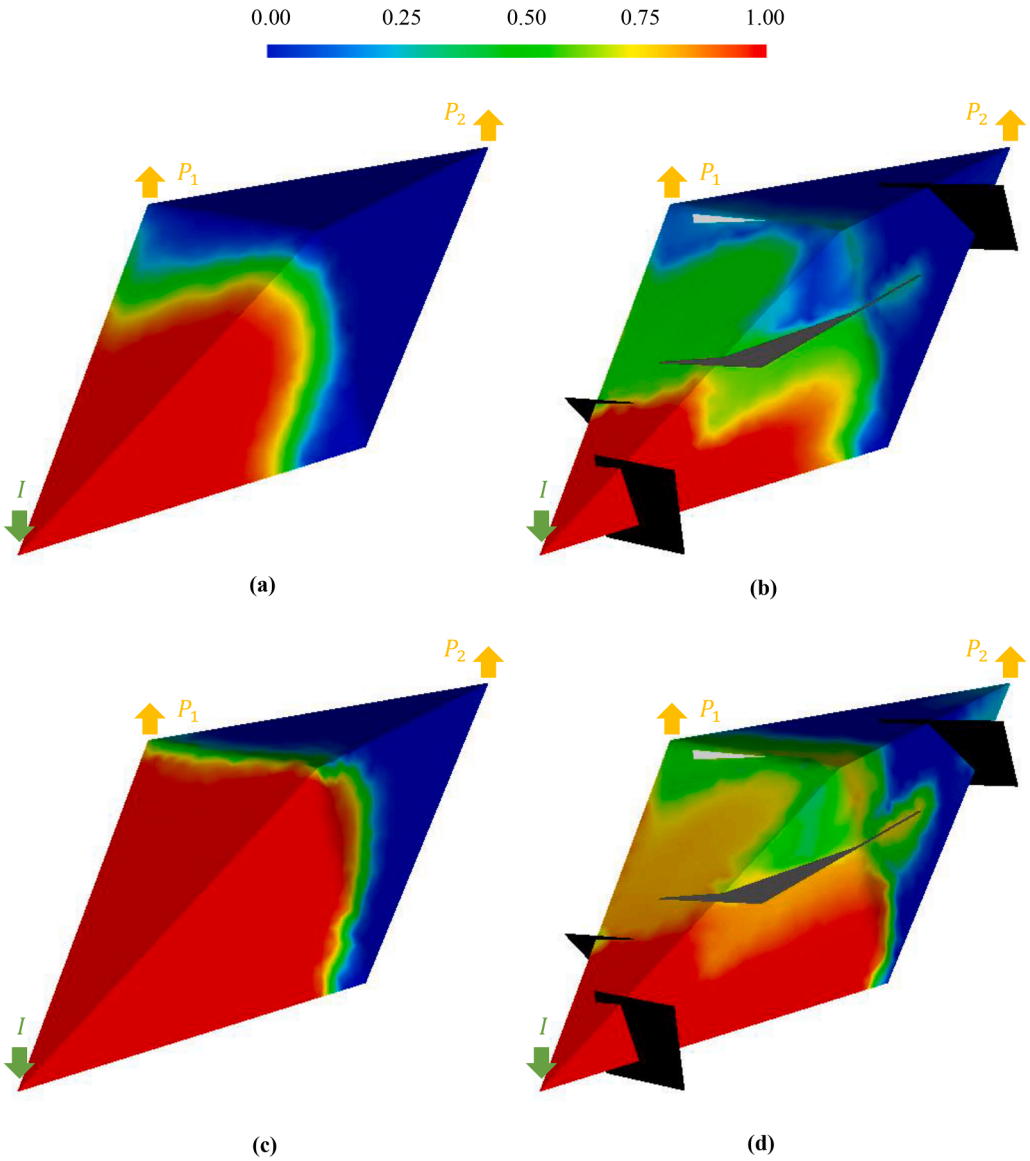

Fig. 18. Water saturation field for test 4.4 - Flow in a Fractured Porous Media with a Full Tensor for the Rock Matrix Permeability in a Non-Cuboid Reservoir. (a) and (c) Fractures are not considered at $t = 231$ days and 500 days, respectively. (b) and (d) Fractures are taken into account at $t = 231$ days and $t = 500$ days, respectively. Black rectangles represent low permeabilities fractures and the white ones represent high permeabilities fractures.

fractures that act as channels, the fluid flows it is accelerated towards the production wells P1 and P2, anticipating the water breakthrough in approximately 60 days in well P1, as it can be seen in Fig. 19b.

Moreover, the Fig. 18d shows that the high permeability fractures conducts the water saturation front to the production well P2 during the first 500 days of injection, what do not happens when the fractures are not considered (Fig. 18c). This is enforced by Fig. 19d, which shows that water production is not perceived in "fractures off" condition, but it is relevant in the "fractures on" condition.

Fig. 19a and Fig. 19c indicate that the cumulative oil productions in P1 and P2 are much larger, when we do not consider fractures with high permeabilities, because, in this case, most of the injected water is channeled to close to the production well, hindering the sweep of the oil throughout the reservoir.

Finally, our strategy, using pEDFM-U and MPFA-D, showed to be able to deal with a full permeability tensor and multiple fractures (channels and barriers), producing physically reasonable solutions, free of non-physical counterflows or any other type of unexpected behavior, which can be concern a whenever using linear MPFA schemes (Cavalcante et al., 2022; Keilegavlen and Aavatsmark, 2011).

4.5. Flow in a highly heterogeneous and anisotropic faulted reservoir

Consider the reservoir as shown in Fig. 20, in which we can see a fault in a porous rock, with a highly heterogeneous permeability field (K_m) defined by Eq. (36) and shown in Fig. 21.

There are two wells, one injector at $\vec{x}_I = (20,\ 50,\ 80)$m with a prescribed pressure $p_I = 0.03$GPa and one producer well at $\vec{x}_P = (150,\ 50,\ 120)$ m with prescribed pressure $p_P = 0.01$GPa.

$$K_m = \begin{bmatrix} y^2+z^2+1 & 0 & 0 \\ 0 & x^2+z^2+1 & 0 \\ 0 & 0 & x^2+y^2+1 \end{bmatrix} .10^{-14}\ \text{m}^2 \tag{36}$$

in which:

$$\begin{cases} x = x/[\max(x) - \min(x)] \\ y = y/[\max(y) - \min(y)] \\ z = z/[\max(z) - \min(z)] \end{cases} \tag{37}$$

The compressibility factors of the fluids are defined as $c_w = 0.4 \cdot 10^{-9}\text{Pa}^{-1}$ (water) and $c_o = 0.6 \cdot 10^{-9}\text{Pa}^{-1}$ (oil). For this problem, we

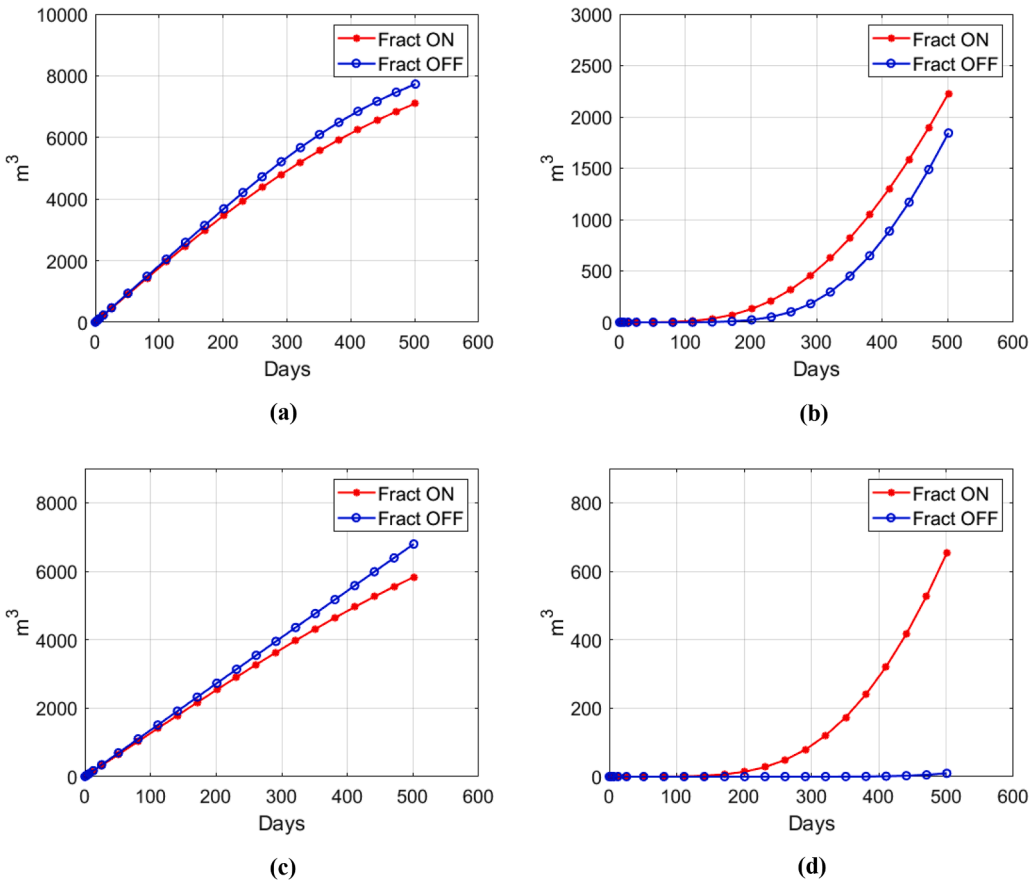

Fig. 19. Cumulative oil and water production for test 4.3 - Flow in a Fractured Porous Media with a Full Tensor for the Rock Matrix Permeability in a Non-Cuboid Reservoir. (a) Cumulative oil production in P1. (b) Cumulative water production in P1. (c) Cumulative oil production in P2. (d) Cumulative water production in P2.

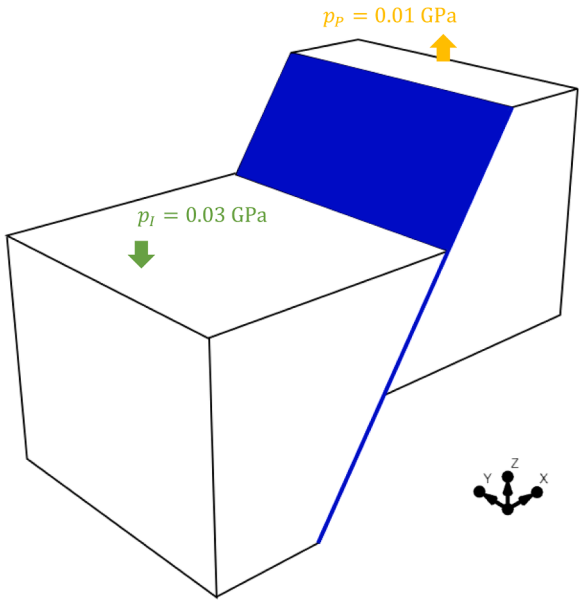

Fig. 20. Geometry, fault and wells positions for the test 4.5 - Flow in a Highly Heterogeneous and Anisotropic Faulted Reservoir. The blue rectangle represents the fault.

consider a tetrahedral mesh with 34,027 CVs discretizing the rock matrix. The fault (or fracture) was discretized by a 2D (38 × 38) with 1444 CVs structured (cartesian) grid and its permeability is given by $K_f = \boldsymbol{I}_{3\times 3}.10^{-6}$ m^2.

The results obtained for the water saturation front are shown in Fig. 22. In Fig. 22b, which is a slice at $y = 50$ m, we can observe that, as expected, in that region, the water saturation front spread preferentially in x direction, if comparing with z direction, and the channel (fault) conducts the water saturation front to close to the production well, which can be seen also in the overview of Fig. 22a. Our formulation, including the pEDFM-U and the MPFA-D, showed to be able to deal with the anisotropy, the high heterogeneity and the faulted characteristic of this reservoir, producing physically reasonable solutions, free of non-physical counterflows or any other type of unexpected behavior, which, as stated before, can be concern a whenever using linear MPFA schemes (Cavalcante et al., 2022; Keilegavlen and Aavatsmark, 2011).

5. Conclusions

We presented the development of a numerical formulation to simulate two-phase flow in naturally fractured heterogeneous and anisotropic reservoirs. For the first time in literature, using a fully implicit implementation, the pEDFM is adapted for use with unstructured tetrahedral meshes (pEDFM-U) using the framework of the software DARSim (Delft Advanced Reservoir Simulation). In our formulation, we inherit the flexibility of modeling complex geometries such as pinchouts, faulted reservoirs, deviated wells, etc., associated to unstructured meshes with the ability of the pEDFM-U to model the effects of both high and low permeability fractures without the necessity to build meshes that fit to the fracture positions, making the mesh generation process simpler and less susceptible to local over refinements.

Through a series of representative problems, we have shown that our formulation is able to handle general tetrahedral meshes and full

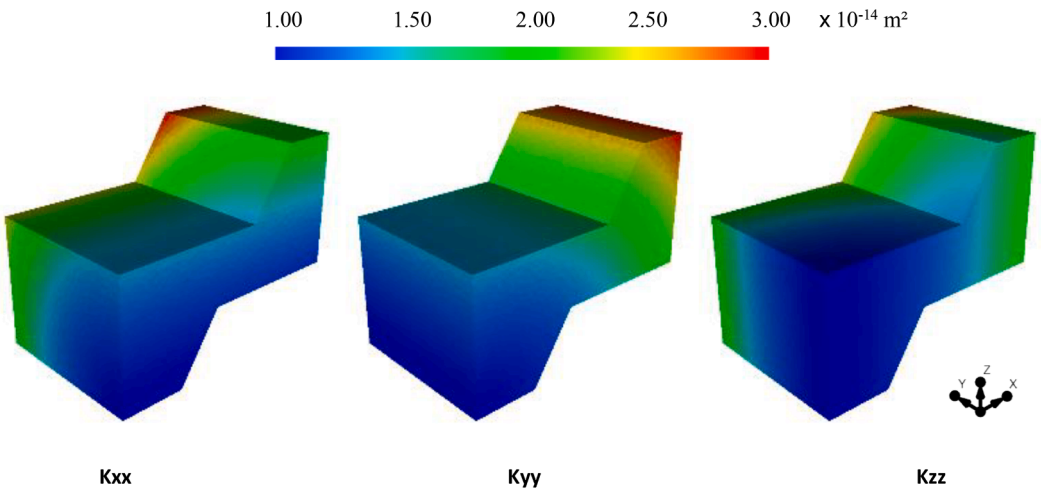

Fig. 21. Permeability distribution for test 4.5 - Flow in a Highly Heterogeneous and Anisotropic Faulted Reservoir.

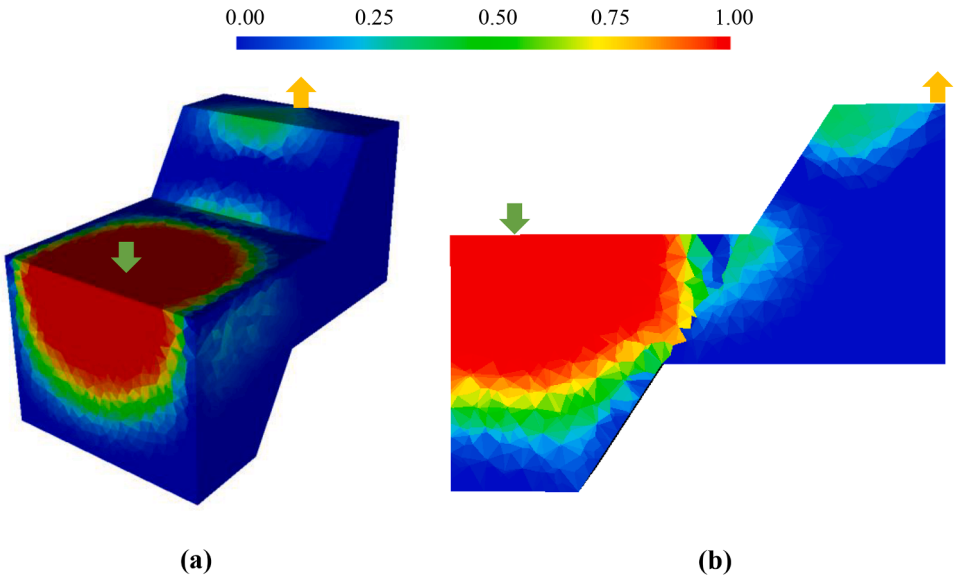

Fig. 22. Water saturation field in test 4.5 - Flow in a Highly Heterogeneous and Anisotropic Faulted Reservoir. (a) Water saturation field at 500 days. (b) Slice at $y =$ 50 m of the water saturation field at 500 days.

permeability tensors, properly reproducing the effects of the presence of both, high and low permeability fractures. Even so, we hope that, in the future, we can complement this study by comparing real field production data. In order to handle real field applications, we intend to further improve our pEDFM-U scheme by integrating it with the recently developed Algebraic Multiscale Scheme for Unstructured Grids (AMS-U) (Souza et al., 2022), allowing to solve large scale problems that would be non-tractable directly on the fine meshes much more accurately than using traditional upscaling techniques. The major challenges we foresee are connected to the extension of the AMS-U to three dimensional applications and to the adaptation of the EDFM-U/pEDFM-U to a multiscale formulation, particularly the difficulty of incorporating fractures in these types of schemes due to necessity of handling fractures and faults that may cross the boundaries of the dual coarse mesh (Tene et al., 2016; Mehrdoost, 2022). In the future, we intend to use our computational strategy to model "real world" applications involving naturally fractured reservoirs, such as the highly heterogeneous and anisotropic carbonate reservoirs that can be found in "Brazilian Pre-Salt (Fernandez-Ibanez et al., 2022; Mendes et al., 2022).

CRediT authorship contribution statement

Túlio de M. Cavalcante: Conceptualization, Methodology, Software, Validation, Formal analysis, Investigation, Data curation, Writing – original draft, Visualization. **Artur C.R. Souza:** Software, Validation, Visualization. **Hadi Hajibeygi:** Supervision, Resources. **Darlan K.E. Carvalho:** Supervision, Resources, Writing – review & editing, Funding acquisition. **Paulo R.M. Lyra:** Supervision, Resources, Writing – review & editing, Project administration, Funding acquisition.

Declaration of competing interest

The authors declare that they have no known competing financial interests or personal relationships that could have appeared to influence the work reported in this paper.

Data availability

Data will be made available on request.

Acknowledgments

The authors thank the Foundation for Support of Science and Technology of Pernambuco (FACEPE), the National Council for Scientific Development (CNPq) and the Coordination for Improvement of Higher Education Personnel (CAPES).

Funding

This work was supported by CNPq (PQ-308334/2019-1 and PQ-310145/2021-0) and FACEPE (IBPG-1160-3.01/18).

References

Aavatsmark, I., Barkve, T., Bøe, Mannseth T, 1998. Discretization on unstructured grids for inhomogeneous, anisotropic media. Part I: derivation of the methods. SIAM J. Sci. Comput. 19, 1700–1716. https://doi.org/10.1137/S1064827595293582.

Aziz, K., Settare, A., 1979. Petroleum Reservoir Simulation. Applied Science Publishers, New York.

Barenblatt, G.I., Zheltov, I.P., Kochina, I.N., 1960. Basic concepts in the theory of seepage of homogeneous liquids in fissured rocks [strata]. J. Appl. Math. Mech. 24, 1286–1303. https://doi.org/10.1016/0021-8928(60)90107-6.

Berre, I., Doster, F., Keilegavlen, E., 2019. Flow in fractured porous media: a review of conceptual models and discretization approaches. Transp. Porous. Media 130, 215–236. https://doi.org/10.1007/s11242-018-1171-6.

Berre, I., Boon, W.M., Flemisch, B., Fumagalli, A., Gläser, D., Keilegavlen, E., et al., 2021. Verification benchmarks for single-phase flow in three-dimensional fractured porous media. Adv. Water. Resour. 147, 103759 https://doi.org/10.1016/j.advwatres.2020.103759.

Carvalho, D.K.E., Willmersdorf, R.B., Lyra, P.R.M., 2009. Some results on the accuracy of an edge-based finite volume formulation for the solution of elliptic problems in non-homogeneous and non-isotropic media. Int. J. Numer. Methods Fluids. 61, 237–254. https://doi.org/10.1002/fld.1948.

Cavalcante, T.M., Lira Filho, R.J.M., Souza, A.C.R., Carvalho, D.K.E., Lyra, P.R.M, 2022a. A multipoint flux approximation with a diamond stencil and a non-linear defect correction strategy for the numerical solution of steady state diffusion problems in heterogeneous and anisotropic media satisfying the discrete maximum principle. J. Sci. Comput. 93, 42. https://doi.org/10.1007/s10915-022-01978-6.

Cavalcante, T.M., Filho, R.J.M.L., Souza, A.C.R., Carvalho, D.K.E., Lyra, P.R.M., 2022b. A Multipoint Flux Approximation with a Diamond Stencil and a Non-Linear Defect Correction Strategy for the Numerical Solution of Steady State Diffusion Problems in Heterogeneous and Anisotropic Media Satisfying the Discrete Maximum Principle. J. Sci. Comput. 93, 42. https://doi.org/10.1007/s10915-022-01978-6.

Cavalcante T de, M., Contreras, F.R.L., Lyra, P.R.M., de Carvalho, D.K.E., 2020. A multipoint flux approximation with diamond stencil finite volume scheme for the two-dimensional simulation of fluid flows in naturally fractured reservoirs using a hybrid-grid method. Int. J. Numer. Methods Fluids. 92, 1322–1351. https://doi.org/10.1002/fld.4829.

Cavalcante T.M. Simulation of immiscible two-phase flow in 3-D naturally fractured reservoirs using a locally conservative method, a projection-based embedded discrete fracture model and unstructured tetrahedral meshes. PhD Thesis, UFPE, 2023.

Chen, Z., Huan, G., Ma, Y., 2006. Computational methods for multiphase flows in porous media. Soc. Ind. Appl. Math. https://doi.org/10.1137/1.9780898718942.

Contreras, F.R.L., Lyra, P.R.M., Souza, M.R.A., Carvalho, D.K.E., 2016. A cell-centered multipoint flux approximation method with a diamond stencil coupled with a higher order finite volume method for the simulation of oil-water displacements in heterogeneous and anisotropic petroleum reservoirs. Comput. Fluids. 127, 1–16. https://doi.org/10.1016/j.compfluid.2015.11.013.

Crumpton, P.I., Shaw, G.J., Ware, A.F., 1995. Discretisation and multigrid solution of elliptic equations with mixed derivative terms and strongly discontinuous coefficients. J. Comput. Phys. 116, 343–358. https://doi.org/10.1006/jcph.1995.1032.

Dershowitz, B., LaPointe, P., Eiben, T., Wei, L., 1998. Integration of discrete feature network methods with conventional simulator approaches. All Days, SPE. https://doi.org/10.2118/49069-MS.

Dong, C., Kang, T., 2021. A least squares based diamond scheme for anisotropic diffusion problems on polygonal meshes. Int. J. Numer. Methods Fluids. 93, 3231–3253. https://doi.org/10.1002/fld.5031.

Dong, C., Kang, T., 2022. A least squares based diamond scheme for 3D heterogeneous and anisotropic diffusion problems on polyhedral meshes. Appl. Math. Comput. 418, 126847 https://doi.org/10.1016/j.amc.2021.126847.

Fernandez-Ibanez, F., Nolting, A., Breithaupt, C.I., Darby, B., Mimoun, J., Henares, S., 2022. The properties of faults in the Brazil pre-salt: a reservoir characterization perspective. Mar. Pet. Geol. 146, 105955 https://doi.org/10.1016/j.marpetgeo.2022.105955.

Gläser D. Case1 - single fracture 2020.

Hajibeygi, H., Karvounis, D., Jenny, P, 2011. A hierarchical fracture model for the iterative multiscale finite volume method. J. Comput. Phys. 230, 8729–8743. https://doi.org/10.1016/j.jcp.2011.08.021.

Hassanpouryouzband, A., Yang, J., Tohidi, B., Chuvilin, E., Istomin, V., Bukhanov, B., 2019. Geological CO $_2$ capture and storage with flue gas hydrate formation in frozen and unfrozen sediments: method development, real time-scale kinetic characteristics, efficiency, and clathrate structural transition. ACS. Sustain. Chem. Eng. 7, 5338–5345. https://doi.org/10.1021/acssuschemeng.8b06374.

Hassanpouryouzband, A., Adie, K., Cowen, T., Thaysen, E.M., Heinemann, N., Butler, I. B., et al., 2022. Geological hydrogen storage: geochemical reactivity of hydrogen with sandstone reservoirs. ACS. Energy Lett. 7, 2203–2210. https://doi.org/10.1021/acsenergylett.2c01024.

HosseiniMehr, M., Vuik, C., Hajibeygi, H., 2020. Adaptive dynamic multilevel simulation of fractured geothermal reservoirs. J. Computat. Phys.: X 7, 100061. https://doi.org/10.1016/j.jcpx.2020.100061.

HosseiniMehr, M., Tomala, J.P., Vuik, C., Al Kobaisi, M., Hajibeygi, H, 2022. Projection-based embedded discrete fracture model (pEDFM) for flow and heat transfer in real-field geological formations with hexahedral corner-point grids. Adv. Water. Resour. 159, 104091 https://doi.org/10.1016/j.advwatres.2021.104091.

Hoteit, H., Firoozabadi, A., 2008. An efficient numerical model for incompressible two-phase flow in fractured media. Adv. Water. Resour. 31, 891–905. https://doi.org/10.1016/j.advwatres.2008.02.004.

Jiang, J., Younis, R.M., 2017. An improved projection-based embedded discrete fracture model (pEDFM) for multiphase flow in fractured reservoirs. Adv. Water. Resour. 109, 267–289. https://doi.org/10.1016/j.advwatres.2017.09.017.

Keilegavlen, E., Aavatsmark, I., 2011. Monotonicity for MPFA methods on triangular grids. Comput. Geosci. 15, 3–16. https://doi.org/10.1007/s10596-010-9191-5.

Li, L., Lee, S.H., 2008. Efficient field-scale simulation of black oil in a naturally fractured reservoir through discrete fracture networks and homogenized media. SPE Reservoir Eval. Eng. 11, 750–758. https://doi.org/10.2118/103901-pa.

Lira Filho, R.J.M., Santos, S.R., Cavalcante, T.M., Contreras, F.R.L., Lyra, P.R.M., Carvalho, D.K.E, 2021. A linearity-preserving finite volume scheme with a diamond stencil for the simulation of anisotropic and highly heterogeneous diffusion problems using tetrahedral meshes. Comput. Struct. 250, 106510 https://doi.org/10.1016/j.compstruc.2021.106510.

Manzocchi, T., Walsh, J.J., Nell, P., Yielding, G., 1999. Fault transmissibility multipliers for flow simulation models. Petrol. Geosci. 5, 53–63. https://doi.org/10.1144/petgeo.5.1.53.

Mehrdoost, Z., 2022. Multiscale finite volume method with adaptive unstructured grids for flow simulation in heterogeneous fractured porous media. Eng. Comput. 38, 4961–4977. https://doi.org/10.1007/s00366-021-01520-6.

Mendes L de, C., Correia, U.M.C., Cunha, O.R., Oliveira, F.M., Vidal, A.C., 2022. Topological analysis of fault network in naturally fractured reservoirs: a case study from the pre-salt section of the Santos Basin. Brazil. J. Struct. Geol. 159, 104597 https://doi.org/10.1016/j.jsg.2022.104597.

Moinfar, A., Narr, W., Hui, M.-H., Mallison, B., Lee, S.H., 2011. Comparison of discrete-fracture and dual-permeability models for multiphase flow in naturally fractured reservoirs. All Days, SPE. https://doi.org/10.2118/142295-MS.

Moinfar, A., Varavei, A., Sepehrnoori, K., Johns, R.T., 2014. Development of an efficient embedded discrete fracture model for 3D compositional reservoir simulation in fractured reservoirs. SPE J. 19, 289–303. https://doi.org/10.2118/154246-PA.

Nilsen, H.M., Lie, K.-A., Natvig, J.R., 2012. Accurate modeling of faults by multipoint, mimetic, and mixed methods. SPE J. 17, 568–579. https://doi.org/10.2118/149690-PA.

Peaceman D.W. Fundamentals of numerical reservoir simulation 1977.

Rao, X., Cheng, L., Cao, R., Jia, P., Liu, H., Du, X., 2020. A modified projection-based embedded discrete fracture model (pEDFM) for practical and accurate numerical simulation of fractured reservoir. J. Pet. Sci. Eng. 187, 106852 https://doi.org/10.1016/j.petrol.2019.106852.

Shakiba M., Sepehrnoori K. Using Embedded Discrete Fracture Model (EDFM) and microseismic monitoring data to characterize the complex hydraulic fracture networks. Day 3 Wed, September 30, 2015, SPE; 2015. https://doi.org/10.2118/175142-MS.

Souza, A.C.R., Carvalho, D.K.E., Santos, J.C.A., Willmersdorf, R.B., Lyra, P.R.M., Edwards, M.G., 2022. An algebraic multiscale solver for the simulation of two-phase flow in heterogeneous and anisotropic porous media using general unstructured grids (AMS-U). Appl. Math. Model. 103, 792–823. https://doi.org/10.1016/j.apm.2021.11.017.

Tene M., Al Kobaisi M.S., Hajibeygi H. Multiscale projection-based Embedded Discrete Fracture Modeling approach (F-AMS-pEDFM), 2016. https://doi.org/10.3997/2214-4609.201601890.

Ţene, M., Bosma, S.B.M., Al Kobaisi, M.S., Hajibeygi, H, 2017. Projection-based Embedded Discrete Fracture Model (pEDFM). Adv. Water. Resour. 105, 205–216. https://doi.org/10.1016/j.advwatres.2017.05.009.

Warren, J.E., Root, P.J., 1963. The behavior of naturally fractured reservoirs. Soc. Petrol. Eng. J. 3, 245–255. https://doi.org/10.2118/426-PA.